การศึกษาปรากฏการณ์โฟโตโวลตาอิกของโครงสร้างนาโนที่ปลูกบนแผ่นฐานแกลเลียมอะเซไนด์ระนาบ (100)

นายองอาจ ตั้งเมตตาจิตตกุล

วิทยานิพนธ์นี้เป็นส่วนหนึ่งของการศึกษาตามหลักสูตรปริญญาวิศวกรรมศาสตรดุษฎีบัณฑิต
สาขาวิชาวิศวกรรมไฟฟ้า ภาควิชาวิศวกรรมไฟฟ้า
คณะวิศวกรรมศาสตร์ จุฬาลงกรณ์มหาวิทยาลัย
ปีการศึกษา 2554

STUDY ON PHOTOVOLTAIC EFFECT OF QUANTUM NANOSTRUCTURE GROWN ON (100) GaAs SUBSTRATE

Mr. Ong-arj Tangmettajittakul

A Dissertation Submitted in Partial Fulfillment of the Requirements

for the Degree of Doctor of Philisophy Program in Electrical Engineering

Department of Electrical Engineering

Faculty of Engineering

Chulalongkorn University

Academic Year 2011

Thesis Title	STUDY ON PHOTOVOLTAIC EFFECT OF QUANTUM NANOSTRUCTURE GROWN ON (100) GaAs SUBSTRATE
By	Mr. Ong-arj Tangmettajittakul
Field of Study	Electrical Engineering
Thesis Advisor	Associate Professor Somchai Ratanathammaphan, D.Eng.
Thesis Co-advisor	Professor Somsak Panyakeow, D.Eng.

Accepted by the Faculty of Engineering, Chulalongkorn University in Partial Fulfillment of the Requirements for the Doctoral Degree

…… Dean of the Faculty of Engineering
(Associate Professor Boonsom Lerdhirunwong, Dr.Ing.)

THESIS COMMITTEE

…….. Chairman
(Professor Charles W. Tu, Ph.D.)

……. Thesis Advisor
(Associate Professor Somchai Ratanathammaphan, D. Eng.)

…….. Thesis Co-advisor
(Professor Somsak Panyakeow, D. Eng.)

…….. External Examiner
(Suwat Sopitpan, Ph.D.)

…….. External Examiner

(Noppadon Nuntawong, Ph.D.)

องอาจ ตั้งเมตตาจิตตกุล : การศึกษาปรากฏการณ์โฟโตโวลตาอิกของโครงสร้างนาโนที่ปลูกบนแผ่นฐานแกลเลียมอะเซไนด์ระนาบ(100). (STUDY ON PHOTOVOLTAIC EFFECT OF QUANTUM NANOSTRUCTURE GROWN ON (100) GaAs SUBSTRATE) อ. ที่ปรึกษาวิทยานิพนธ์หลัก : รศ.ดร. สมชัย รัตนธรรมพันธ์, อ. ที่ปรึกษาวิทยานิพนธ์ร่วม : ศ.ดร. สมศักดิ์ ปัญญาแก้ว, 87 หน้า.

วิทยานิพนธ์นี้นำเสนอผลการศึกษาปรากฏการณ์โฟโตโวลตาอิกในโครงสร้างนาโนได้แก่ โครงสร้างควอนตัมด็อทโมเลกุลความหนาแน่นสูงอินเดียมอาร์เซไนด์บนผลึกฐานแกลเลียมอาร์เซไนด์ด้วยกระบวนการปลูกผลึกแบบ Stranski-Krastanov growth mode และ โครงสร้างควอนตัมรูปวงแหวนของอินเดียมแกลเลียมอาร์เซไนด์บนอะลูมิเนียมแกลเลียมอาร์เซไนด์ ด้วยเทคนิคการปลูกผลึก Droplet epitaxy โดยประดิษฐ์ขึ้นจากการปลูกผลึกอิพิแทกซีจากลำโมเลกุล (Molecular Beam Epitaxy)

โครงสร้างควอนตัมด็อทโมเลกุลหนาแน่นสูงอินเดียมอาร์เซไนด์ ได้วิเคราะห์อิทธิพลของจำนวนชั้นที่มีผลต่อสมบัติทางไฟฟ้า และทำการเปรียบเทียบผลกับโครงสร้างควอนตัมด็อทโดยได้เปรียบเทียบสมบัติทางแสง ซึ่งแสดงให้เห็นว่าการเปล่งแสงของโครงสร้างควอนตัมด็อทโมเลกุลความหนาแน่นสูงให้โฟตอนที่มีค่าพลังงานสูงกว่าและให้ผลตอบสนองต่อความยาวคลื่นที่กว้างกว่าโครงสร้างควอนตัมด็อทแบบปกติ อย่างไรก็ตามคุณสมบัติทางไฟฟ้าจากงานวิจัยนี้ยังไม่สามารถบ่งชี้ได้ชัดเจนว่าการใช้โครงสร้างโมเลกุลความหนาแน่นสูงนั้นจะให้ผลที่ดีกว่า

สำหรับโครงสร้างควอนตัมรูปวงแหวนของอินเดียมแกลเลียมอาร์เซไนด์ ได้ทำการศึกษาเงื่อนไขตัวแปรการประดิษฐ์ที่มีผลต่อโครงสร้างควอนตัมรูปวงแหวนของอินเดียมแกลเลียมอาร์เซไนด์อาร์เซไนด์ จากนั้นนำเงื่อนไขการปลูกที่ได้มาประดิษฐ์โครงสร้างขนาดใหญ่และมีค่าหนาแน่นสูงสุด โดยประดิษฐ์โครงสร้างหลายชั้นเพื่อทำให้ได้ค่าความหนาแน่นสูง เนื่องจากโครงสร้างที่ได้มีค่าความหนาแน่นผลวิเคราะห์ทางแสงพบว่าโครงสร้างขนาดใหญ่ให้การเปล่งแสงที่ค่าโฟตอนที่มีพลังงานต่ำกว่า ซึ่งแสดงให้เห็นได้ชัดเจนกว่าโครงสร้างที่มีความหนาแน่นสูงกว่า อย่างไรก็ตามโครงสร้างนี้ไม่แสดงผลตอบสนองทางแสงที่เพิ่มขึ้นเมื่อเทียบกับตัวอย่างอ้างอิงที่ไม่มีโครงสร้างนาโน ในขณะที่โครงสร้างควอนตัมรูปวงแหวนให้ความหนาแน่นสูงให้ผลทางแสงที่ดีขึ้น โดยคุณสมบัติทางไฟฟ้าของโครงสร้างควอนตัมรูปวงแหวนให้ผลที่ดีกว่าตัวอย่างอ้างอิงที่ไม่มีโครงสร้างนาโน

ภาควิชา วิศวกรรมไฟฟ้า ลายมือชื่อนิสิต.....

สาขาวิชา วิศวกรรมไฟฟ้า ลายมือชื่อ อ.ที่ปรึกษาวิทยานิพนธ์หลัก.....

ปีการศึกษา 2554 ลายมือชื่อ อ.ที่ปรึกษาวิทยานิพนธ์ร่วม .....

5071827821 : MAJOR ELECTRICAL ENGINEERING

KEYWORDS : InAs / InGaAs / GaAs / NANOSTRUCTURES / QUANTUM DOT / QUANTUM DOT MOLECULE / QUANTUM RING / MOLECULAR BEAM EPITAXY / SK GROWTH MODE / DROPLET EPITAXY / PHOTOVOLTAIC CELL

ONG-ARJ TANGMETTAJITTAKUL : STUDY ON PHOTOVOLTAIC EFFECT OF QUANTUM NANOSTRUCTURE GROWN ON (100) GaAs SUBSTRATE, ADVISOR : ASSOC. PROF. SOMCHAI RATANATHAMMAPHAN, D.Eng., CO-ADVISOR : PROF. SOMSAK PANYAKEOW, D.Eng , 87 pp.

This thesis presents a study on the photovoltaic effect of quantum nanostructures grown on (100) GaAs substrate. The nanostructures in this work are InAs high-density-quantum-dot-molecule (HD-QDM) and InGaAs quantum ring (QR). The fabrication techniques are Stranski-Krastanov growth mode for HD-QDM and droplet epitaxy for InGaAs quantum ring (QR). A molecular beam epitaxy system is used as the fabrication tool.

The stacking number of HD-QDM structure is optimized by I-V characteristic. Then, the selected structure is compared with a conventional QD structure in optical and electrical properties. Photoluminescence shows that HD-QDM structure gives a higher energy peak position than QD structure. It also gives a broader spectral response than QD structure. However, it cannot be concluded that HD-QDM has a better electrical properties than QD structure.

In the case of QR structure, GaAs/AlGaAs QRs have been fabricated with various growth conditions in order to investigate the effect of fabrication parameters on the structural properties. Then, the selected growth condition is used to obtain the highest density and largest size nanostructures for InGaAs QR structure. In order to increase the density, multi-stack InGaAs QRs are used to increase the density of InGaAs QRs. The large QR size gives PL spectrum a clearer and lower energy peak than the other sample with higher density. However, the large QRs do not give an extra spectral response when compared with a non-QR reference sample, whereas the other sample does. The QR structure also gives a better I-V characteristic than the reference sample.

Department : Electrcal Engineering	Student's Signature .....
Field of Study : Electrcal Engineering	Advisor's Signature .....
Academic Year : 2011	Co-advisor's Signature .....

Acknowledgements

I would like to give special thanks to my family for encouraging support in my work. I gratefully thank you to Assoc.Prof. Dr. Somchai Ratanathammaphan, and Prof. Dr. Somsak Panyakeow who are advisors. In this work, it will be unsuccessful, if I do not have valuable chance, importance advice, and guidance from my advisors.

I would like to acknowledge to other lecturers of the Semiconductor Device Research Laboratory (SDRL), Assoc. Prof. Dr. Choompol Amtarasena, Assoc. Prof. Dr. Montri Sawadsaringkarn, Assoc. Prof. Dr. Banyong Toprasertpong, Assoc. Prof. Dr. Songphol Kanjanachuchai, and Dr. Chanin Wissawinthanon. I also would like to thank you to Mr. Supachok Thainoi for his help and kindness for assisting photoluminescence measurement. I thank to others staff, Mr. Pornchai Changmoang, Mr. Pattana Phuntuwong, Mrs. Kwanruan Thainoi and Mrs. Banditha Ratwiset, for cheerfulness in my work. I would like to deep acknowledge to my seniors, Dr. Suwit Kiravittaya and Dr. Suwaree Suraprapapich, for their suggestion and advice.

I would like to thank you to member of the thesis committee, Porf. Dr. Charles W. Tu, Dr. Suwat Sopitpan, and Dr. Noppadon Nuntawong. I would like to thanks all of my friends in SDRL, Dr. Wipakorn Jewasuwan, Dr. Poonyaseri Boonpeng, Dr. Naraporn Pankaow, and colleagues for discussion, suggestion and helpful. Finally, I have to give special thanks to Thailand Research Fund (TRF) through the Royal Golden Jubilee Ph.D. Program (Grant no. PHD/0017/2552), DPG380002, National Nanotechnology Center (NANOTEC) of Thailand, Higher Education Research Promotion, National Research University Project of Thailand, and Office of the Higher Education Commission (EN264A) for financial support.

CONTENTS

Page

Page

LIST OF FIGURES

Page

Page

Page

Page

LIST OF SYMBOLS

∇^2	Laplacian operator
τ_C	lifetime associated to other nonradiative recombination mechanisms between the CB and the IB
τ_V	lifetime associated to other nonradiative recombination mechanisms between the IB and the VB
β	Current gain factors
η	efficiency
δ	delta function
$\lambda_{de\ Broglie}$	de Broglie wavelength
Θ	angle
a.u.	arbitrary unit
A	area
AFM	atomic force microscopy
Al	aluminium
AlAs	aluminium arsenide
AlGaAs	aluminium gallium arsenide
Ar^+	argon ion
As	arsenic
As_4	arsenic
Au	gold
AuZn	gold zinc
AuGe/Ni	gold germanium nickel
BEP	beam equivalent pressure
c_A	Auger & impact ionization component
CB	conduction band
D	diode
DE	droplet epitaxy
D.O.S.	density of state
DMM	digital multi-meter

DQR	double quantum ring
$D_{bulk}(E)$	density of state of bulk structure
$D_{QD}(E)$	density of state of quantum dot structure
D_K	diode with contribute from impact ionization and Auger mechanisms
$D_{QW}(E)$	density of state of quantum well structure
$D_{QWR}(E)$	density of state of quantum wire structure
eG_{CV}^{ext}	contribution by CB to VB region
eG_{CI}^{ext}	contribution by IB to CB region
eG_{IV}^{ext}	contribution by VB to IB region
eG_{EN}	contribution by the front emitter
eG_{EP}	contribution by the rear emitter
$E_{l,x}$	quantized energy in x-direction
$E_{m,y}$	quantized energy in y-direction
$E_{n,z}$	quantized energy in z-direction
F.F.	fill factor
F(r)	envelope wave function
FM	Frank-van der Merve
FWHM	full width at half maximum
Ga	gallium
GaAs	gallium arsenide
GaInP	gallium indium phosphide
GaP	gallium phosphide
GaNAs	gallium nitrogen arsenide
h	Planck's constant
$\bar{h}$	reduced Planck's constant
HD-QDM	high density quantum dot molecule
IBSC	intermediate band solar cell
IB	intermediate band
In	indium

InAs	indium arsenide
InGaAs	indium gallium arsenide
InP	indium phosphide
J	net current density
J_{dark}	dark current density
$J_{L,CV}$	photocurrent of the transitions from the VB to the CB
$J_{L,CI}$	photocurrent generated from IB to CB
$J_{L,IV}$	photocurrent generated from VB to IB
J_0	reverse saturation current density
J_m	maximum current density
J_{sc}	photocurrent density at short circuit
k	wave vector of carriers
k_B	Boltzmann's constant
Lx	nanometer length scale in x direction
Ly	nanometer length scale in y direction
Lz	nanometer length scale in z direction
m^*	effective mass
m_{eq}	equilibrium electron concentration in IB.
MBE	molecular beam epitaxy
MEE	migration enhanced epitaxy
ML	monolayer
MOCVD	metal organic chemical vapor deposition
n_{eq}	equilibrium electron concentration in CB
N_D	volume density of quantum dot
N_{wi}	area density of quantum wire
p_{eq}	equilibrium hole concentration in VB.
P_s	incident light
p	carrier momentum
P	power density
PBN	pyrolytic boron nitride
PMT	photomultiplier tube

q	electron charge
QD	quantum dot
QDM	quantum dot molecule
QR	quantum ring
QW	quantum well
QWR	quantum wire
R_s	series resistance
R_{sh}	shunt resistance
RHEED	reflection high-electron energy diffraction
SI	semi insulator
Si	silicon
SiGe	silicon germanium
SK	Stranski Krastanow
T	temperature
VB	valence band
V_m	maximum voltage
V_{oc}	open circuit voltage
$V(r)$	potential barrier
VW	Volmer-Weber
W	thickness of IB region

CHAPTER I

INTRODUCTION

1.1 Historical Background and Motivation

The development of energy technology is used to compensate the oil crisis in 1973. Many alternative ways have been used to produce energy such as wind energy, nuclear energy, coal energy, solar energy, etc. However, in 1986 and 2011, the world met disasters from nuclear power plants. Therefore, green energy such as solar energy is one of the most interesting alternatives. The first solar cell was invented in 1883 by Charles Fritts, who coated the semiconductor selenium with an extremely thin layer of gold to form junctions. After this period, Si was the most interesting material to study and fabricate solar cells [1-3]. Not only crystalline Si but also poly-crystalline Si and amorphous Si was used in solar cell fabrication [4-6]. Nevertheless, Si is not the best selection in term of energy conversion because of two facts, i.e. the bandgap of Si does not fit to the highest peak of the solar spectrum and Si is an indirect bandgap semiconductor. These lower photo-current conversion effectiveness. GaAs is another semiconductor material, of which the bandgap matches to the highest peak of the solar spectrum. In addition, GaAs also has a direct bandgap. These properties can lead to efficient absorption of GaAs-based solar cells.

However, the maximum theoretical efficiency of a single p-n junction solar cell, calculated by William Shockley and Hans Queisser, is limited to 33% [7]. Therefore, several strategies for increasing the Shockley-Queisser limit have been proposed. Tandem solar cells, hot carrier solar cells, impact ionization solar cells, and intermediate band solar cells have been introduced [8-12]. Among them, tandem solar cells and intermediate band solar cells have been experimentally reported by Takamoto *et al*., Luque *et al*.. The tandem solar cells or multi-junction solar cells have been developed in a variety of material combinations in order to utilize different photon energies in solar cells. To date, the efficient tandem cellhave efficiency of more than 43.5% such as

GaInP/GaAs/GaInNAs triple junction cell systems [13]. Although the tandem cell can improve the quantum efficiency of solar cells, there are many difficulties in fabrication techniques such as tunnel junctions, lattice constant of materials, and current matching. By the way, intermediate band solar cell, a type of single junction solar cells, is another alternative way. The intermediate band solar cells have been proposed by Luque *et al.* Intra-band state, introduced by impurities in the semiconductor, is one of the intermediate band ideas for multi-absorption. However, the isolated impurities may act as non-radiative recombination centers which can reduce the efficiency. Therefore, another approach is using low-dimensional semiconductor heterostructures as an intermediate band structure.

Low-dimensional structures such as quantum well (QW), quantum dot (QD), and quantum ring (QR) can be used as active-layers of solar cells. Bamham *et al.* proposed the first two-dimensional QW application in a p-i-n solar cell. However, QW structures are quite unsuitable for the intermediate band structures because of their continuous density of state (DOS). Therefore, carriers in this structure can be scattered to lower band by phonon interaction. To resolve this, Luque *et al.* has proposed the use of zero-dimensional QD structures as intermediate band of solar cells. The predicted efficiency of the QD intermediate band solar cell is up to 63% [12]. Moreover, in 2011, Nozawa and Arakawa had shown the maximum theoretical efficiency up to 80% [14] by increasing the number of intermediate levels. Therefore, using zero-dimensional nanostructures in solar cells, the experimental efficiency can be potentially increased.

QD, a type of zero-dimensional nanostructures, can exhibit many unique interesting properties such as discrete energy levels, high optical nonlinearly, and δ-function-like density of states [15] which are the required concepts of intermediate band solar cell. There are two main approaches for QD fabrication; i.e. “top-down” and “bottom-up”. Via top-down method, QDs are fabricated by patterning. The advantages of this technique are controllable size and position arrangement. Despite many advantages, this method is rather complicated and can cause defects which lead to degradation of device properties. Another approach is “bottom-up”, or self-assembly

method, which has been used to fabricate QDs in this research work. This technique, referred as Stranski-Krastanov (SK) growth mode [16], originates by strain of heteroepitaxial growth in lattice-mismatched material systems such as Si/Ge and In(Ga)As/GaAs [17-20]. Among many material systems, the In(Ga)As/GaAs QD system is widely used in numerous intermediate band solar cell researchs due to its energy band structures and opto-electronic properties. Sugaya *et al.* and Sablon *et al.* have reported In(Ga)As/GaAs QD solar cells that give more extended spectral response in the infra-red region and also a large short circuit current (I_{sc}), compared with solar cells without QDs. Although the In(Ga)As/GaAs QDs can give an enhancement of solar cells, they can create strain-defects due to stacking of QDs which is used for increasing QD density (QDs per area or volume). To resolve this problem, Nuntawong *et al*., Hubbard *et al*., Okada et al. have introduced strain compensation in multi-stacks QDs by using compound semiconductors with different lattice-constant like GaInP, GaP,GaNAs [21-23] as a spacing layer with appropriate thicknesses to compensate the accumulating stain in stacking layers. However, the multi-stacking of QDs is not easy in practical due to long processing steps.

For another method to increase QDs per volume, Surapprapich *et al.* have fabricated high-density quantum dot molecules (HD-QDMs) by using a capping-and-regrowth technique [24, 25]. The density of HD-QDM is higher than that of conventional QDs by about one order of magnitude. In this dissertation, therefore, the fabrications of multi-stack InAs QD and HD-QDM as active layers in the InAs/GaAs(100) system have been demonstrated by Stranski-Krastanov (SK) growth mode using molecular beam epitaxy (MBE) for comparison.

Although several researchers of InAs/GaAs QDs reported an enhancement of spectral response and short circuit current (I_{sc}), the open circuit voltage (V_{oc}) has a severe drop [26-29]. There are many discussions on the drop of V_{oc}. However, Guimard *et al.* (2010) and Antolín *et al.* (2010) have demonstrated and explained how to improve V_{oc}. Bailey *et al.* (2011) have demonstrated a small drop in V_{oc} and enhancement of I_{sc}.

In their experiment, V_{oc} is improved to 0.994 V [30]. They proposed that typical loss in V_{oc} was induced from localized strain defects.

In this dissertation, another nanostructure system was applied in solar cells. Lattice-matched GaAs/AlGaAs and low-mismatched GaInAs are proposed by droplet epitaxy technique [31-33]. The motivation for making use of the very low lattice-mismatched Ga(In)As/AlGaAs structures is to improve the V_{oc} of quantum nanostructure solar cells. After the quantum ring (QR) growth, the surface morphology of the QRs was analyzed by using an atomic force microscope (AFM). Photoluminescence (PL) measurement was performed to characterize the optical properties of the QRs. For QR solar cells, spectral response was performed to characterize the optical properties of the solar cells. I-V characteristic was also performed to analyze the electrical properties of the solar cells.

1.2 Objective

The objective of this dissertation is to fabricate InAs high-density quantum dot molecules (HD-QDMs) and Ga(In)As quantum rings (QRs). Surface morphologies of the HD-QDMs and the QRs using solid-source molecular beam (MBE) have been characterized by atomic force microscopy (AFM). Photoluminescence (PL) and spectral response measurement have been analyzed for their optical properties. The HD-QDMs and the QRs have been inserted in solar cell structures to study the effects of nanostructures inserted in p-i-n solar cells.

1.3 Overview

This dissertation presents a study of the InAs/GaAs HD-QDM and GaAs/AlGaAs QR insertion in p-i-n solar cells using molecular beam epitaxy (MBE). The purpose is to analyze the structural, optical, and electrical properties of the devices.

This thesis is arranged into 6 chapters. Chapter 1 is introduction, motivation and a brief review of QD solar cell literatures. In chapter 2, the basic rational concept of low-dimensional nanostructures along with the concept of self-assembled QDs, self-

assembled QRs, and the basic concept of intermediate band solar cell are introduced. Chapter 3 provides experimental details, including experimental procedures and characterization processes. For the results and discussions, they consisted of two parts. The first part, chapter 4, discusses experimental results of physical, optical, and electrical properties of InAs/GaAs HD-QDM structures and application in p-i-n solar cells. The multi-stacked HD-QDM structure is optimized for using in photovoltaic cells. Surface morphologies and optical properties are observed by atomic force microscopy (AFM) and photoluminescence (PL). I-V characteristic and spectral responses are analyzed to evaluate their electrical properties. The second part is an investigation with different nanostructures. In chapter 5, experimental results of surface morphology, optical, and electrical properties of Ga(In)As/AlGaAs QR structures applied to p-i-n solar cells are discussed. In addition, the electrical properties of several different nanostructures are compared in this section. Finally, chapter 6 is the conclusion of this thesis.

CHAPTER II

REVIEW OF BASIC CONCEPT

This chapter provides the basic concept of solar cell, low-dimensional nanostructures and intermediate band solar cell. Self-assembled growth techniques, including Straski-Krastanow (SK) and droplet epitaxy, are explained to give an understanding of quantum dot (QD) and quantum ring (QR) formation mechanisms. The high density quantum dot molecules growth by the thin-capping-and-regrowth technique is also described in this chapter.

2.1 Basic concept of solar cell

Solar cell or photovoltaic cell is a device which converts light (photon) energy to electrical energy. Normally, solar cell is a p-n junction device which has a shallow junction. Due to this junction, the solar cell can be considered as a diode in the dark and a dc battery when it is illuminated by sun light. When light is incident on a solar cell, electron-hole pairs are generated by photon energy which is higher than the bandgap of the solar cell. By the electric field in the transition region of the junction, minority carriers from p-type (electrons) and from n-type (holes) are separated and forced to move into the opposite sites. This effect induces a reduction of the potential barrier at the junction and causes the open circuit voltage (V_{oc}) as shown in Figure 2.1.

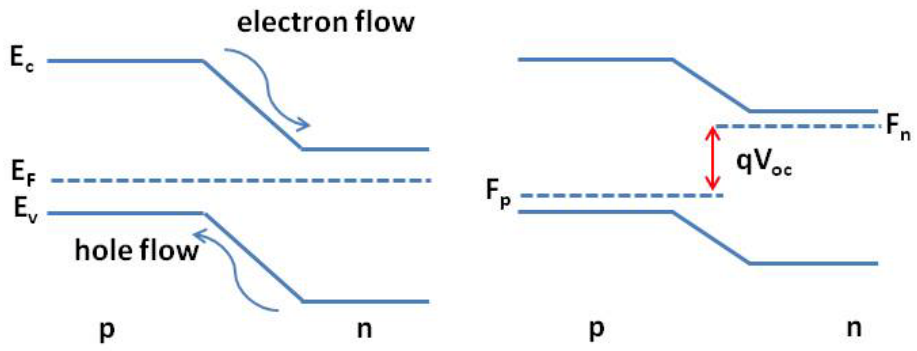

Figure 2.1 Energy diagram of p-n junction solar cell

Photocurrent is also produced by the illuminated light. The photocurrent density in short circuit (J_{sc}) depends on the intensity of the incident light. When a solar cell is connected to a load, a potential difference is formed between the terminals of the device. This potential difference generates a current. However, the net current is reduced from its short circuit value. This reverse current is called the dark current. For ideal diode, the dark current density (J_{dark}) is

$$J_{dark} = J_0(e^{\frac{qV}{kBT}} - 1) \tag{2.1}$$

where J_0 is the reverse saturation current density, k_B is Boltzmann's constant and T is temperature in Kelvin.

Therefore, the net current density under illumination is

$$J = J_{sc} - J_0(e^{\frac{qV}{kBT}} - 1) \tag{2.2}$$

Practically, the power is dissipated through parasitic resistances which are resulted from contacts and leakage currents of both sides. The series resistance (R_s) is resulted from resistance of the cell material, and it affects the current flow. The shunt resistance (R_{sh}) is from leakage current through the cell. The equivalent circuit of solar cell is shown in Figure 2.2.

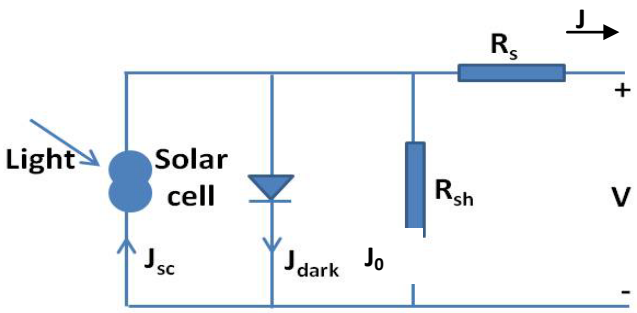

Figure 2.2 Equivalent circuit of a solar cell including series and shunt resistance.

When combining the effect of these parasitic resistances, the diode equation is now rewritten to

$$J = J_{sc} - J_0(e^{\frac{q(V+JAR_s)}{kBT}} - 1) - (V + JAR_s)/R_{sh} \quad (2.3)$$

The working regime of a solar cell is the range of bias from 0 to V_{oc}. The power density (P) of the device is given by

$$P = JV \quad (2.4)$$

Therefore, P reaches the maximum power point at maximum voltage (V_m) with a corresponding maximum current density (J_m), as shown in Figure 2.3.

The efficiency (η) of the cell is defined by the power density delivered at the operating point as a function of incident light power P_s.

$$\eta = J_m V_m / P_s = J_{sc} V_{oc} FF / P_s \quad (2.5)$$

where the Fill factor (FF) is defined following equation 2.5.

$$FF = J_m V_m / J_{sc} V_{oc} \quad (2.6)$$

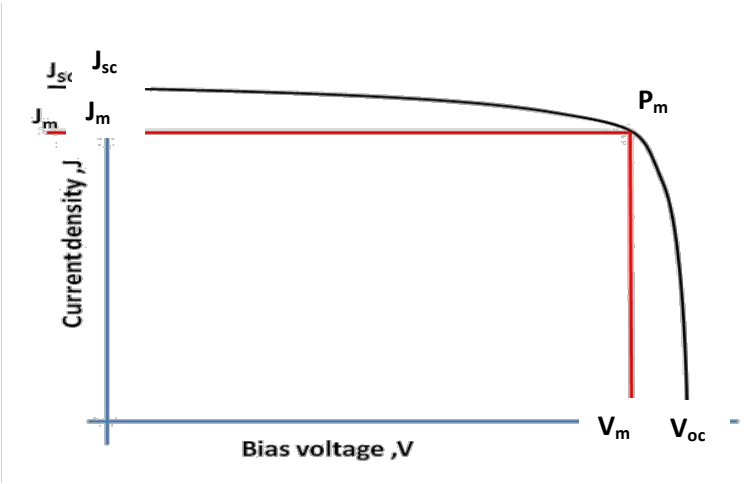

Figure 2.3 Current-voltage (J-V) characteristic of solar cell

However, there are many factors that affect the solar cell efficiency such as material bandgap and contact loss. As mentioned in chapter 1, Shockley and Queisser have calculated the solar cell efficiency limit of 33 % for GaAs. In the next section, intermediate band solar cell, which is to overcome the solar cell efficiency limit, is briefly introduced.

2.2 Intermediate band solar cell

Recently, many researchers [34-37] work to enhance the maximum efficiency limit of a solar cell. Intermediate band solar cell (IBSC), which was proposed by Luque *et al.* , is one approach to extend the efficiency limit. The idea of the IBSC is to introduce a partially occupied intermediate band (IB) level between the valence band (VB) and conduction band (CB) of the active region in a cell. Three different absorption processes are available in such a system thereby increasing the photocurrent by the additional transition from VB to IB and from IB to CB absorption. Figure 2.4 presents a band diagram of the IBSC.

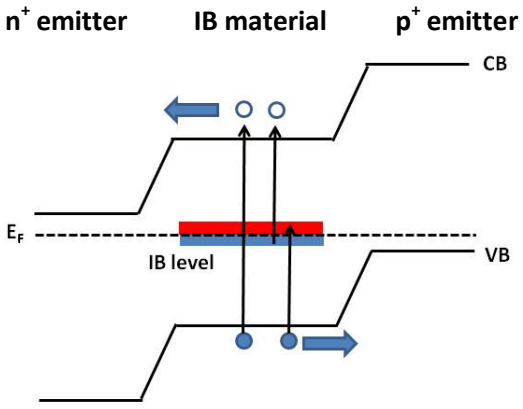

Figure 2.4 Energy band diagram of the solar cell with intermediate level has been sandwiched between two emitters.

The generalized equivalent circuit for the IBSC was also proposed by Luque *et al.* It is composed of a photocurrent source in parallel with a diode representing VB to CB pumping and recombination. In parallel with this host sub-cell, there is a series

combination of two further sub-cells, representing pumping and recombination for the VB to IB and the IB to CB transitions. The equivalent circuit of IBSC is shown in Figure 2.5. All the parameters of the equivalent circuit and their relationship to their physical origin are described in reference [26].

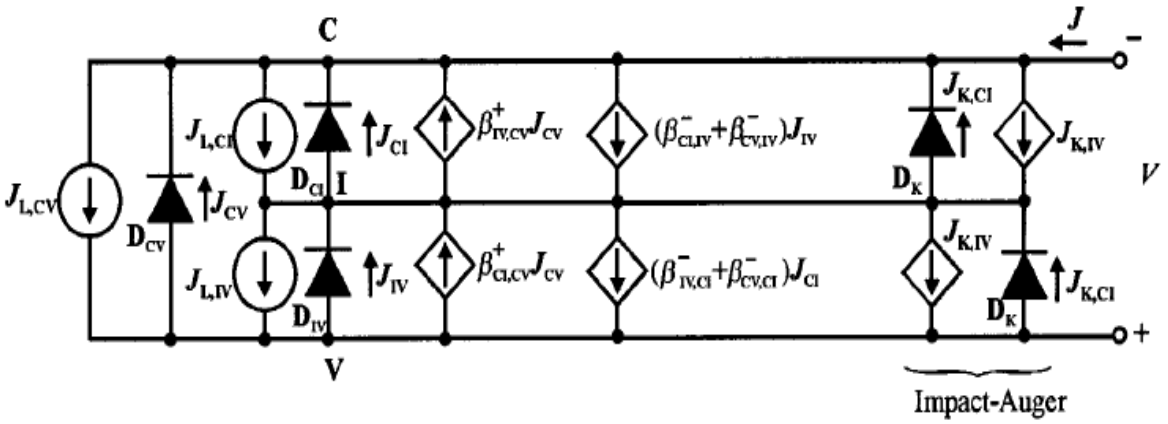

Figure 2.5 Equivalent circuit of an intermediate band solar cell combining the effect from impact ionization and Auger recombination phenomena [26].

Total contribution to the photocurrent of the transitions from the VB to the CB :

$$J_{L,CV} = eG_{CV}^{ext} + eG_{EN} + eG_{EP} \qquad (2.7)$$

where eG_{EN} is the contribution by the front emitter; eG_{EP} is the contribution by the rear emitter; eG_{CV}^{ext} is the contribution by CB to VB region.

IB to CB photogenerated current :

$$J_{L,CI} = eG_{CI}^{ext} \qquad (2.8)$$

VB to IB photogenerated current :

$$J_{L,IV} = eG_{IV}^{ext} \qquad (2.9)$$

Diodes D_{xy} reverse saturation current where *xy* is substituted by *CV, CI* and *IV* :

$$J_{0,CV} = J_{CV,CV}^{ext} + J_{0,N} + J_{0,P} \quad (2.10)$$

$$J_{0,CI} = J_{CV,CI}^{ext} + J_{CI,CI}^{ext} + J_{JV,CI}^{int} + en_{eq}W/\tau_C \quad (2.11)$$

$$J_{0,IV} = J_{CV,IV}^{ext} + J_{CI,IV}^{int} + J_{IV,IV}^{ext} + ep_{eq}W/\tau_V \quad (2.12)$$

where $J_{0,N}$ is the contribution from recombination in the front emitter; $J_{0,P}$ is the contribution from recombination in the rear emitter; $en_{eq}W/\tau_C$ is the contribution from other non-radiative recombination mechanisms between the CB and the IB; $ep_{eq}W/\tau_V$, contribution from other non-radiative recombination mechanisms between the IB and the CB.

Reverse saturation current for diodes D_K which corresponds to impact ionization and Auger mechanisms

$$J_{0,K} = ec_A\ P_{eq}m_{eq}^2U/A \quad (2.13)$$

Current gain factors:

$$\beta_{a,b}^{\pm} = (J_{a,b}^{int} \pm J_{c,b}^{ext})/J_{0,b} \quad (2.14)$$

with *a*, *b*, *c* taking the values *CI*, *IV*, or *CV*.

The doping impurities into a silicon cell is the first experiment for testing IBSC concept [38-39]. However, this approach was expected to achieve small efficiency improvements [12]. Later, the focus is switched to low-dimensional nanostructure for forming the IB. The low-dimensional nanostructures are quantum well (QW), quantum wire (QWR), quantum dot (QD), and quantum ring (QR) which will be described in the next section. AlGaAs/GaAs multi-QW was the first low- dimensional structure applied to

solar cell device [40]. Nevertheless, thermodynamic treatments of these devices by Luque *et al.* have shown that QW solar cells cannot improve upon this limit unless electron-hole-pairs in the QW absorb low energy photons to escape out of the wells. Therefore, lower dimensional structures such as QD and QR are focused to form the IB. Several research groups have experimentally demonstrated some of the QD-IBSC operation [41-45]. They are fabricated mostly by self-assembled growth in Stranski-Krastanow (SK) growth mode. The detail of SK growth mode is described in section 2.4. A requirement of the QD IBSC is a high density of QDs. However, the density of conventional In(Ga)As QD is not enough. To increase the dot density for efficient optical absorption, the In(Ga)As/GaAs QD structures have to be fabricated in multi-stacking.

Although, there are several reports on the advantage of QD solar cells with a wider spectral response and more J_{sc} than non-QD-integrated solar cells [47-49], the QD solar cells still have unacceptable low V_{oc} [27-30], as shown in Figure 2.6.

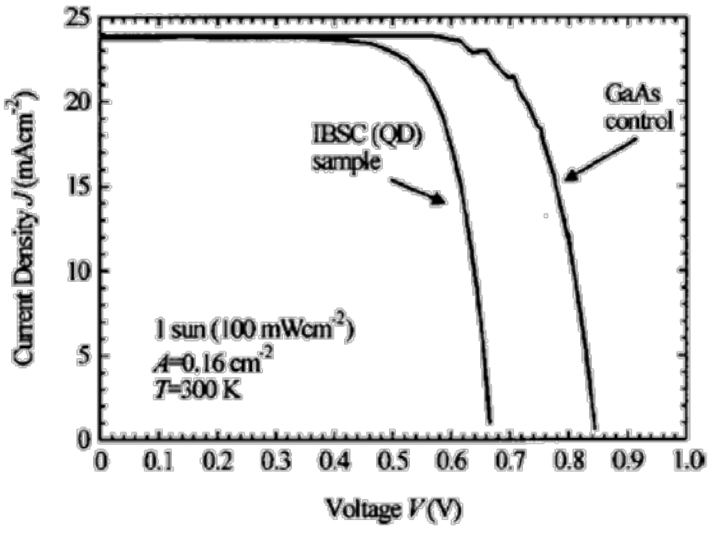

(a)

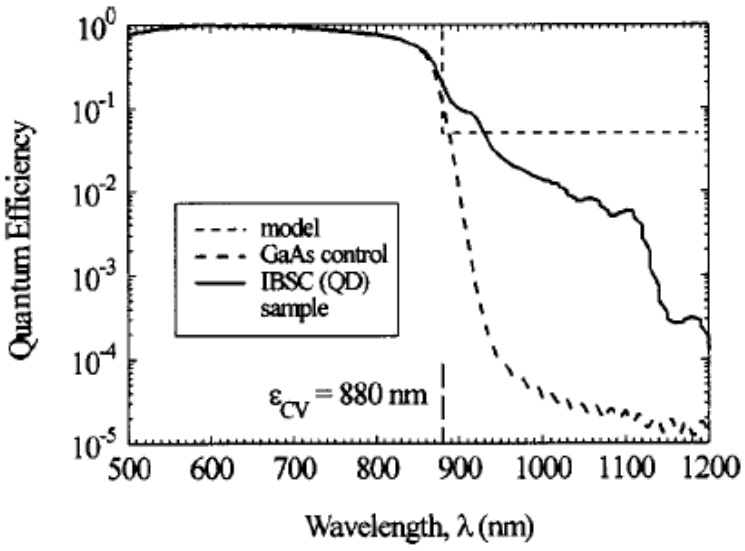

(b)

Figure 2.6 Comparison between the GaAs control sample and InAs QD solar cells (a) I-V characteristic under one sun illumination (b) Quantum Efficiency [26].

As mention in chapter 1, this phenomenon is due to the residual strain and quasi Fermi level of QD states [30, 49]. Many research groups solve this problem by insertion of strain-compensated materials such as GaInP, GaP, GaNAs [21-23]. However, this technique is quite complicated. Therefore, this research studies high density quantum dot molecule (HD-QDM) and QR as IB material. The HD-QDM structure is fabricated by a thin-capping-and regrowth process, which is described in section 2.5. QR structure is fabricated by droplet epitaxy which is described in section 2.6.

2.3 Low dimensional structures

The freedom of carrier movement is limited when the size of the crystal is reduced to nano-meter scale of the order of the carrier's de Broglie wavelength, as shown in equation 2.7, and when the crystal is encircled by other crystals acting as barriers. QDs are low-dimensional semiconductor nanostructure in which carriers are confined in all 3 dimensions. Thus, the energy levels are quantized (Figure 2.7).

$$\lambda_{de\ Broglie} = \frac{h}{p} = \frac{h}{\sqrt{3m^* k_B T}} \quad (2.15)$$

where h is Planck's constant, p is carrier momentum, and k_B is Boltzmann' constant.

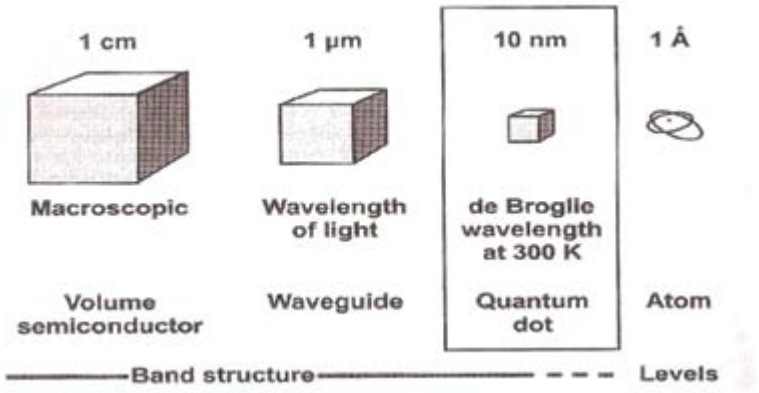

Figure 2.7 Schematic typical dimensions of bulk material, waveguides for visible light, quantum dots and atoms [16].

The electronic structure is analyzed in the terms of density of state (D.O.S.). The D.O.S. of QDs is modified from the continuous distribution in bulk materials to a discrete distribution like delta-function (Figure 2.8). The D.O.S. consists of a series of peaks corresponding to the discrete eigen-energies of electrons. Because of their discrete energy, much like an atom, QDs are called artificial atoms.

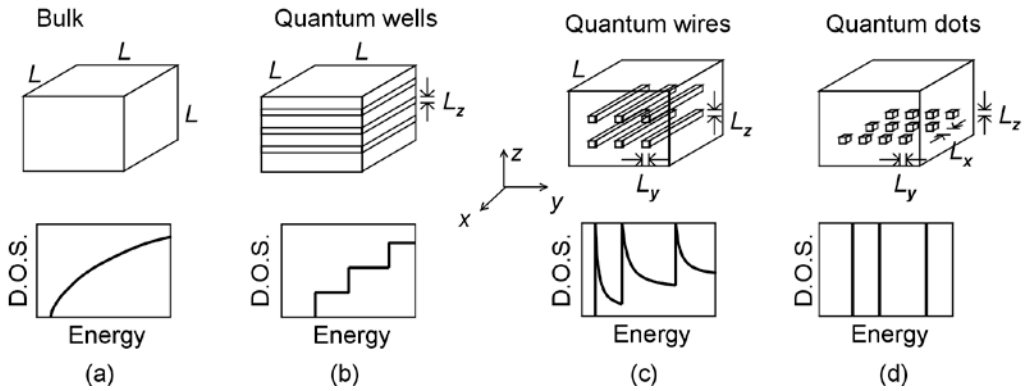

Figure 2.8 Schematic views and graphs of (a) bulk, (b) QWs, (c) QWRs, and (d) QDs and their density of states (D.O.S.). *L* is in macroscopic scale (~cm), while L_x, L_y, L_z, are in nanoscale [50].

The effective mass approximation (m*) can describe the electronic states of bulk semiconductor (Wolfe *et al*.). In quantum well structure, this approximation is widely used for the calculation of quantized energy level. The main assumption of m* is applied to all low- dimensional nanostructures as illustrated in Figure 2.8. Band-edge electron states of semiconductors can be explained by the Schrodinger equation

$$\left[\left[-\frac{\bar{h}^2}{2m^*}\right]\nabla^2 + V(r)\right]F(r) = EF(r) \qquad (2.16)$$

where *V*(r) is the potential barrier, *F*(r) is the envelope wave function and *E* is the carrier energy.

From equation (2.16), the carrier energy in the case of bulk, quantum well (QW) quantum wire (QWR) and QD can be written as

$$\mathrm{E_{QW}} = \mathrm{E(k)} = \frac{\bar{\mathrm{h}}^2 \mathrm{k_{//}}^2}{2\mathrm{m}^*} + \mathrm{E_{n,z}} \qquad (2.17)$$

$$E_{QWR} = E(k) = \frac{\bar{h}^2 k_{\perp}^{\ 2}}{2m^*} + E_{m,y} + E_{n,z} \quad (2.18)$$

$$E_{QD} = E_{l,x} + E_{m,y} + E_{n,z} \quad (2.19)$$

Where $k = (k_x, k_y, k_z)$ is the wave vector of carriers; $k^2 = k_x^{\ 2} + k_y^{\ 2} + k_z^{\ 2}$, $k_{//}^{\ 2} = k_x^{\ 2} + k_y^{\ 2}$, and $k_{\perp} = k_x^{\ 2}$.

The energy $E_{l,x}$, $E_{m,y}$, $E_{n,z}$ which depend on quantum number l, m, n are a function of the potential barrier V(r). The D.O.S. of each structures is written as

$$D_{bulk}(E) = \frac{1}{2\pi^2}\left[\frac{2m^*}{\bar{h}^2}\right]^{3/2} E^{1/2} \quad (2.20)$$

$$D_{QW}(E) = \frac{2m^*}{\pi\bar{h}^2}\sum_n \Theta(E - E_{n,z}) \quad (2.21)$$

$$D_{QWR}(E) = \frac{N_{wi}}{\pi}\frac{\sqrt{2m^*}}{\bar{h}}\sum_{m,n}\frac{1}{\sqrt{E - E_{m,y} - E_{n,z}}} \quad (2.22)$$

$$D_{QD}(E) = 2N_D \sum_{l,m,n} \delta(E - E_{l,x} - E_{m,y} - E_{n,z}) \quad (2.23)$$

Semiconductor QD structures can be fabricated by several techniques, such as lithographic patterning, and self-organization [16]. The fabrication by self-organization gives the formation of defect-free QDs which provide good optical and electrical properties. The QD fabrication details in this thesis are described in section 2.4.

2.4 Quantum dot fabrication techniques

Generally, there are several techniques to produce QD such as synthesize by chemical methods in colloidal semiconductor, by lithographic techniques and by self-

assembled growth in Stranski-Krastanov (SK) growth mode and by droplet epitaxy. However, self-assembled QD by SK growth mode is used in this research. In this section is also explained the growth process of HD-QDM formation and explained the droplet epitaxy which is used for quantum ring formation.

2.4.1 Formation of quantum dot by SK growth mode

In order to describe the SK growth mode, stress, strain and total surface energy are considered. In lattice-matched systems, the growth mode is solely governed by the interface and surface energies. If the total of the epilayer surface energy and the interface energy is lower than energy of substrate surface, the Frank Van de Merwe (FM) growth mode occurs (Figure 2.9(a)). A change in surface energy and interface energy alone may drive a transition from the FM to Volmer-Weber (VW) growth mode (Figure 2.9(b)). A strained epilayer with small interface energy, initial growth may occur layer by layer, but a thicker layer has a large strain energy and can be lower its energy by forming isolated islands in which of strain is relaxed. Thus, the Stranski-Krastanov (SK) growth mode occurs (Figure 2.9(c)).

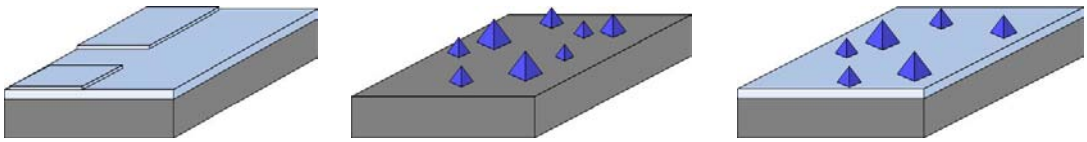

(a) (b) (c)

Figure 2.9 Schematic representation of the three crystal growth modes (a) Frank Van de Merwe (FM) (b) Volmer-Weber (VW) and (c) Stranski-Krastanov (SK)

The SK growth mode which is formed by strained heteroepitaxy, is a widely used method to fabricate QD structure. QDs can be fabricated by molecular beam epitaxy (MBE) or metal organic chemical vapor deposition (MOCVD). By depositing a few

monolayers (MLs) of lattice mismatch material the QDs form. During the growth process, elastic strain energy is created. In order to increase the film thickness to the critical thickness, the system has to release this strain energy by change the growth mode from 2D to 3D growth mode, causing island nucleation. The schematic representation of the local strain energy density of SK growth mode is illustrated in Figure 2.10.

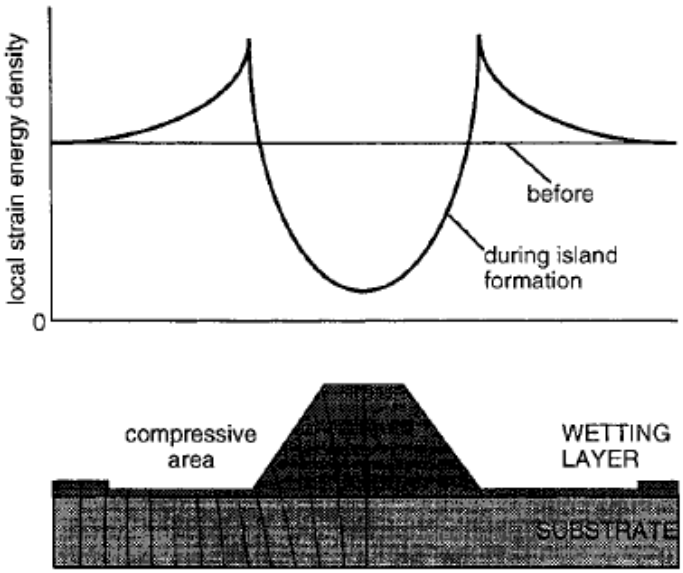

Figure 2.10 Schematic representation of the local strain energy density of SK growth mode [51].

As a result in reference [52], it reports on the growth rate effect on size distribution and dot density. However, the dot density is increased as a function of growth rate, the dot uniformity is decreased. Thus, in this thesis is used low In deposition rate to form QD structure. Also, in this thesis is used thin-capping-and-regrowth process to form HD-QDM, which can increase the dot density.

2.4.1.1 Thin-capping-and-regrowth-technique for HD-QDM [24, 25]

In this section, the thin-capping-and-regrowth-technique for high QD density is described. This technique was developed by Suraprapapich et al. The QDM structure is driven by anisotropic strain fields between the thin capping layer and the as-grown QDs.

The growth process of QDMs is started by growing 1.8 ML InAs QDs at 500ºC. Then, the substrate temperature is decreased to 470ºC and buried QDs with 6 ML of GaAs. After this step, the thin-capped InAs QDs are transformed to nanohole-camel-like structure. The regrowth of InAs QDs on nanoholes are performed at the same temperature with 0.6 ML and transformed to QDs with propeller shape. With more InAs amount, the QDs with nano-propeller are transformed to QDMs. In order to increased QDM density, the QDM formation process is repeated for multiple cycles. At the last cycle, 1.5 ML InAs is required to form HD-QDM structure. AFM images showing the evolution from QDs to HD-QDMs are illustrated in Figure 2.11.

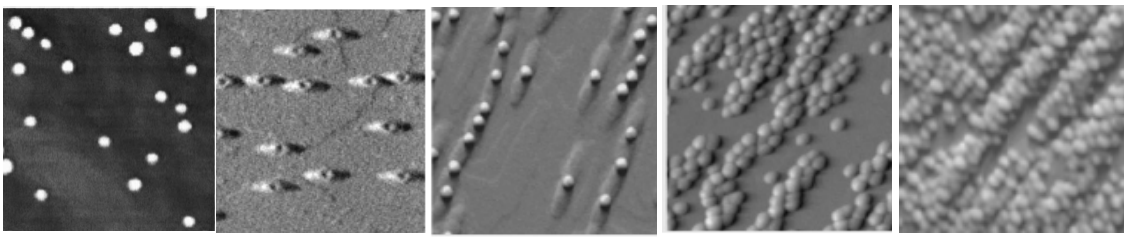

(a) (b) (c) (d) (e)

Figure 2.11 The AFM images show transformation process from as grown QD to HD-QDM by thin-capping-and-regrowth process [24,25] (a) as-grown QD, (b) nanohole-camel-like, (c) QD with propeller shape, (d) QDM and (e) HD-QDM.

2.4.2 Droplet Epitaxy

Droplet epitaxy is another fabrication technique of self-assembled nanostructure. It can be used to both lattice-matched and lattice-mismatched systems. The nanostructures fabricated by this technique are originated from strain-free group III-column element droplets formed on substrate surface instead of strain relaxation in the SK growth mode system. Thus, unstrained nanostructures can be fabricated by the droplet epitaxy. This technique is also low-temperature process, comparing to the SK growth mode. By using droplet epitaxy, ti is possible to fabricate a variety of

nanostructures such as QD, QR, concentric double QR, concentric triple QR, QDM and coupled ring/disk [31-33, 53-55]. This variety comes from the growth parameters such as substrate temperature, deposition thickness of group III-column element, flux pressure of group V-column element and crystallization temperature.

The droplet epitaxy mainly consists of two step processes. First, group III-column element is initially supplied and spontaneously created droplets on substrate surface without of group V-column flux. In this step, droplet formation mechanism of group III-column element is described by VW or SK growth mode. Second step, the group V-column element flux is used for the crystallization of group III-column droplets into III-V compound nanostructures. The illustration of nanostructure fabrication process by droplet epitaxy is represented in Figure 2.12. As mentioned in low temperature process, capping process also required low temperature in order to prevent the nanostructure transformation. Migration enhanced epitaxy is a growth technique for capping the nanostructure. This technique will explain in the next section.

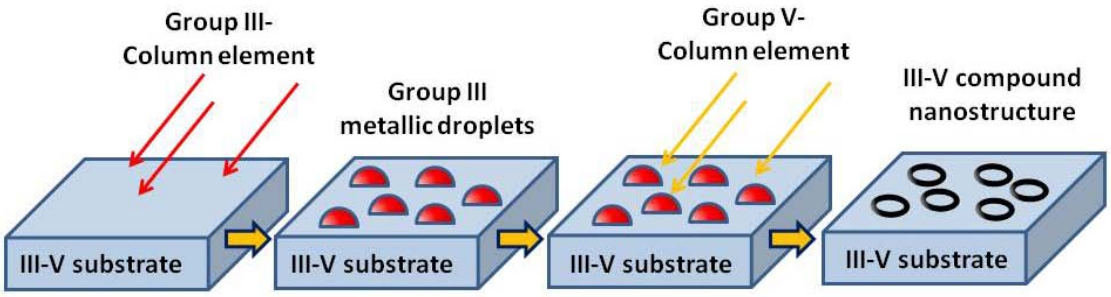

Figure 2.12 Schematic illustration of the nanostructure fabrication process by droplet epitaxy.

2.4.3 Migration Enhanced Epitaxy

Migration enhanced epitaxy (MEE) is useful technique for high quality epitaxial growth at low substrate temperature. MEE is based on the rapid surface migration effect which is characteristic of group III-column atoms in a group V-column-free atmosphere.

In MEE growth process, interruption of the shut off group V supply to growing surface while the group III supply is an essential to the migration enhancement of the adatom. Thus, the group III and group V are alternately supplied to the substrate to obtain metal-stabilized surfaces periodically. The grown layer is formed layer-by-layer. The result shows that a better surface flatness is obtained by MEE. This is most caused by the migration of group III atom on the surface.

The MEE growth has been applied for reduction of oval defect on GaAs surface [56]. It also beneficially effects in the growth of GaAs on Si substrate [57]. This technique can reduce the defect density near the GaAs/Si interface.

CHAPTER III

EXPERIMENTAL DETAILS

This chapter gives the details of sample fabrication procedure by molecular beam epitaxy. The in situ observation via reflection high-energy electron diffraction (RHEED) was used for growth rate calibration and surface structure observation in this work. Surface morphology and optical properties of the samples are characterized by the ex situ observation i.e., atomic force microscope (AFM), photoluminescence (PL) measurement, and spectral response measurement. Ohmic contact and Schottky contacts are also prepared to characterize electrical properties and spectral response of the samples.

3.1 Molecular Beam Epitaxy

Molecular beam epitaxy (MBE) is one of favorite technique for III-V compound semiconductor growth. High quality crystal layer is produced by molecular beams of the elements in clean and ultra high vacuum (UHV) conditions. The high performance device can be fabricated from this system because it can precisely control growth parameters i.e., thickness, doping concentration and composition, etc.

In this research, a solid source MBE RIBER 32P machine consisting of four chambers, i.e., load-lock chamber, introduction chamber, transfer chamber, and growth chamber is used to fabricate all samples. Four chambers are separated by isolation gate valves and one can transfer the samples by magnetic arms. Load-lock chamber is a chamber to load/unload sample from/to atmospheric environment to/from vacuum. In the load-lock chamber has a turbo molecular pump to keep the vacuum in the chamber. Next three chambers have the pumping systems including a ion pump and a titanium sublimation pump to keep the UHV condition. In introduction chamber, there is a heater as called “preheat station” for pre-treatment process of substrate. A propose of preheat is to remove some contaminated substances, moisture, from substrate surface,

molybdenum block. A figure of RIBER 32P MBE is shown in Figure 3.1. The pressure of each chamber is monitored by ionization gauge. The substrate is rotated continuously during growth to provide uniform flux profile on substrate surface. The group III-elements, i.e., In, Ga and Al, group IV ,i.e., Si and group V-elements, i.e., As_4 are contained in pyrolytic boron nitride (PBN) crucibles which are installed in the separated effusion cells. Each cell is heated by its own heater of which temperature is controlled by feedback from standard thermocouple via computer. The molecular beam flux of each constituent element is controlled by tantalum shutter in front of each cell. A schematic drawing of the modified III-V MBE growth chamber is shown in Figure 3.2.

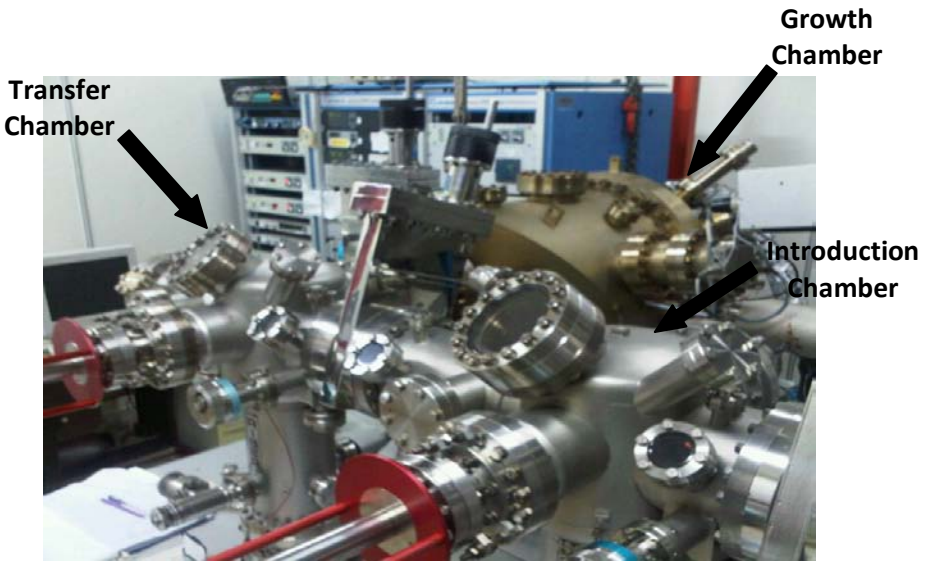

Figure 3.1 RIBER 32P Molecular beam epitaxy machine.

The advantage of MBE over the other growth techniques is that it enables to study and control the growth process in situ by analyzer equipment. In particular, reflection high-energy electron diffraction (RHEED) allows directly monitor the surface structure of the sample and the already grown epilayer. The explanation on RHEED is presented in the next section. In addition, the quadruple mass spectroscopy is also installed to analyze the particle in growth chamber.

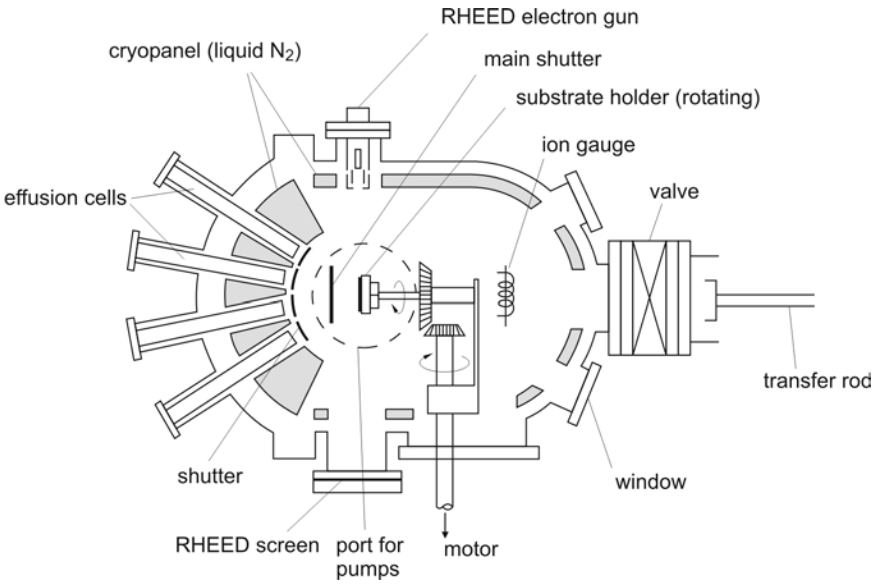

Figure 3.2 Schematic drawing of the conventional III-V MBE growth chamber. The chamber is cooled by a liquid N_2. The base pressure is less than 1×10^{-10} torr [58].

3.2 Reflection high-energy electron diffraction (RHEED)

Reflection high-energy electron diffraction is an in-situ equipment for monitoring the surface morphology during growth in MBE system. It simple has only electron gun, a phosphor screen, and substrate surface. The schematic representation of RHEED system is shown in Figure 3.3. A high-energy electron beam (10-30 keV) reflects by the sample surface at smallw angle (θ ~1-3°) because it is diffracted by the surface atoms, which function as grating. The RHEED pattern would be captured with a high-performance CCD camera and analyzed with data processing software installed to the computer.

The RHEED pattern can be determined by used of Ewald construction in the reciprocal lattice. This imaging observation method is called Laue method. In the case of smooth surface, the reciprocal lattice is composed of rods in the reciprocal space in perpendicular direction to the real surface. When the surface is roughness, the surface layer in the reciprocal space will be demonstrated by a three-dimensional point array. Thus, the RHEED pattern can be interpreted as the reciprocal lattice of the sample

surface, which reflects the surface morphology on the atomic scale. In this thesis, RHEED observation is used for growth rate calibration, substrate surface temperature calibration and during growth observation.

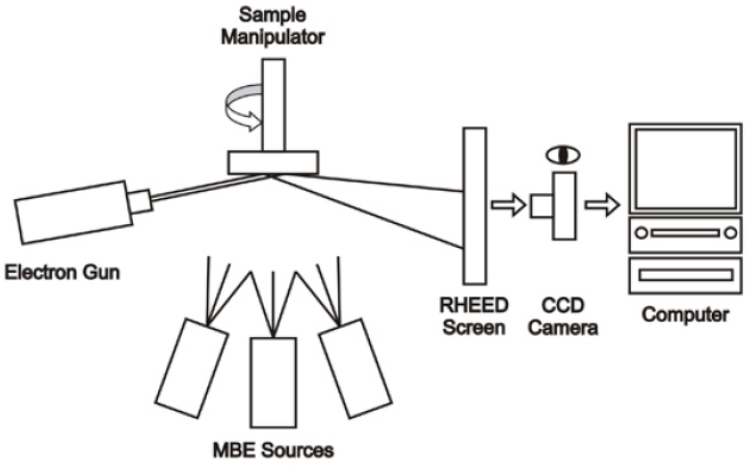

Figure 3.3 Schematic representation of RHEED system.

In order to calibrate substrate temperature, the transition of the reconstruction pattern as a function of substrate temperature is used to determine. In the case of GaAs (100), the transition from (2x4) to c(4x4) point is used to be a reference point. In this thesis, this transition temperature is at 500ºC under As_4 beam pressure of $8x10^{-6}$ Torr. When the substrate temperature is decreased, RHEED pattern along the [1-10] direction changes the transition point from (2x4) to c(4x4). Figure 3.4 shows the RHEED pattern which change from (2x4) to c(4x4) by ramping temperature down. To define the substrate temperature at 500ºC, we record four transition temperature values from thermocouple, T_1, T_2, T_3 and T_4. T_1 is recorded when secondary line at the center disappears. When the same line appear, the pattern change to c(4x4) and T_2 is recorded. T_3 and T_4 are recorded by increasing the temperature and recording at reverse transition pattern of T_2 and T_1, respectively. The average value of T_1, T_2, T_3 and T_4 is used as reference temperature of 500ºC. Figure 3.5 illustrates the transition temperature process of calibration GaAs temperature and the RHEED pattern which correspond to transition temperature value.

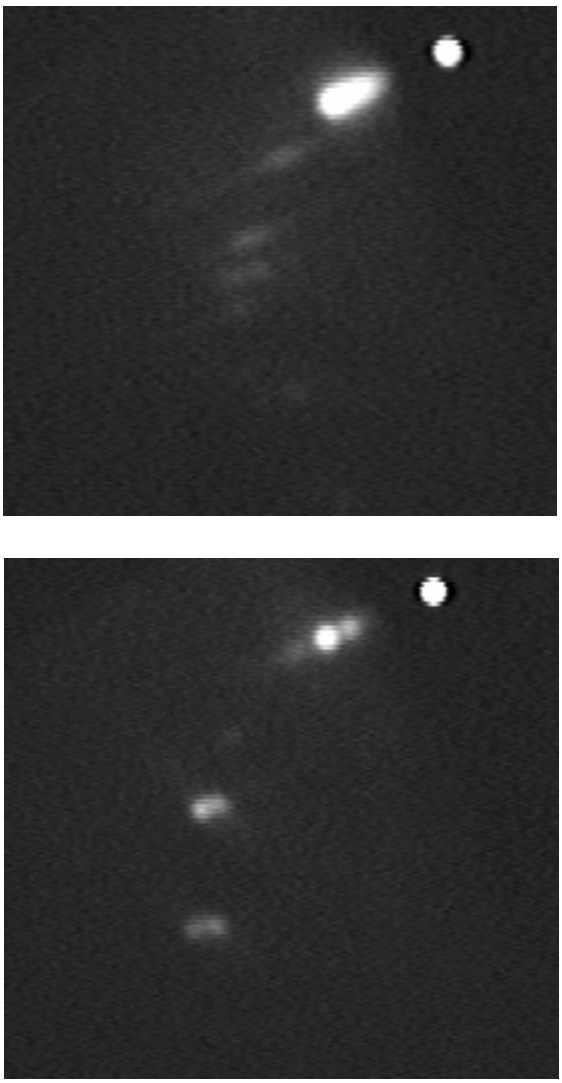

Figure 3.4 RHEED pattern changes from (2x4) to c(4x4) by changing temperature down.

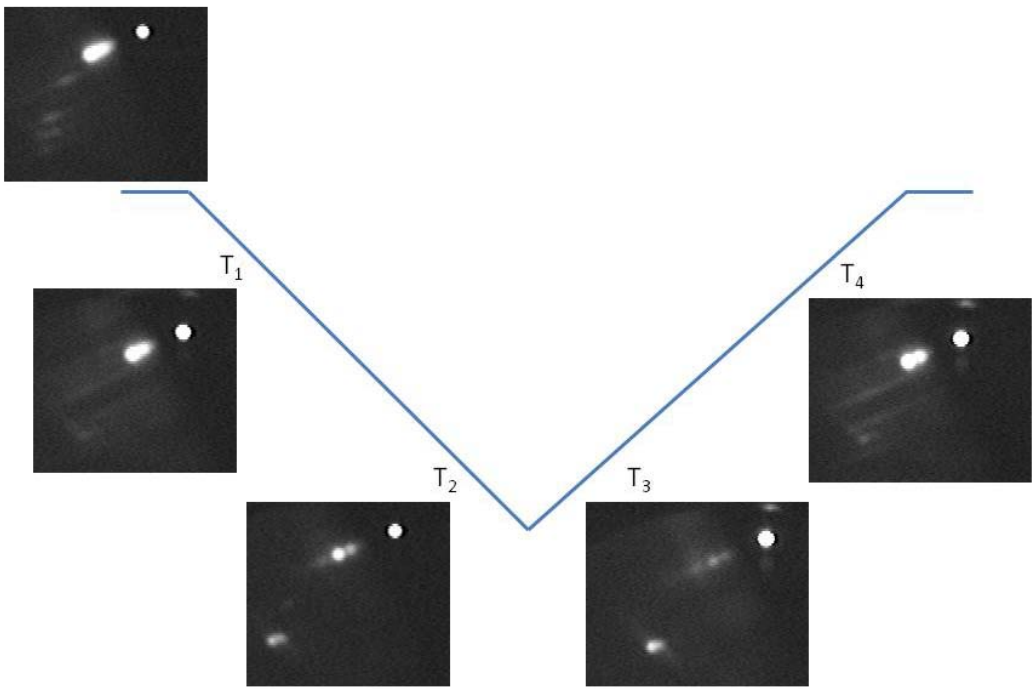

Figure 3.5 Transition temperature processes of calibration GaAs temperature and the corresponding RHEED pattern.

RHEED intensity oscillations are applied to determine the growth rate deposition. The growth of atomic layer is completed layer-by-layer. From this fact, if the layer is not completed, it is not to be smooth surface. Thus, the RHEED intensity is oscillated as a function of surface roughness. A period of RHEED intensity oscillation corresponds to 1 ML of each layer such as GaAs, AlAs and AlGaAs. The RHEED oscillation frequency indicates to the growth rate of each material. A schematic representation of the RHEED intensity oscillation is illustrated in Figure 3.6.

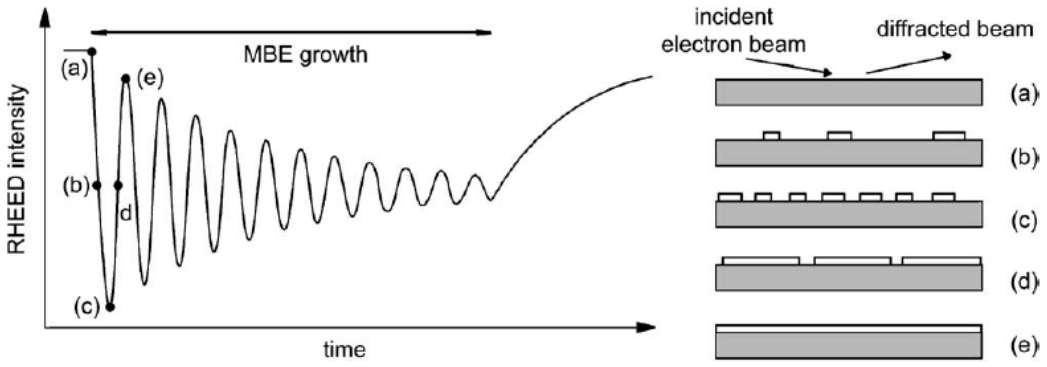

Figure 3.6 Illustration of layer-by-layer growth by nucleation of 2D islands and the corresponding intensity of the zero-order diffracted RHEED beam [59].

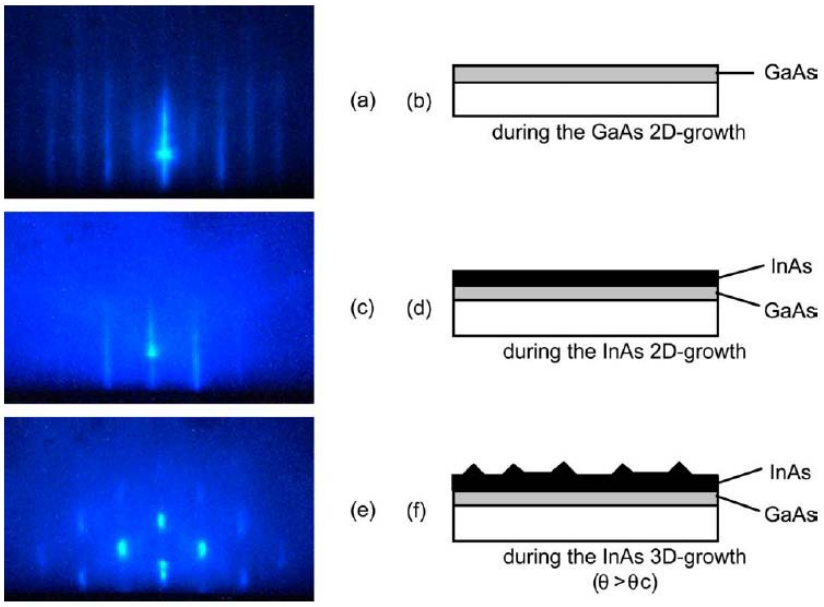

Figure 3.7 The RHEED pattern transition during the growth InAs on GaAs surface which corresponds to changing pattern from steaky pattern to spotty pattern [59].

Generally, the RHEED observation allows us to continuously monitor the surface growth. In S-K growth mode, when 3-D islands are formed by the strain relaxation, the

RHEED pattern changes from streaky to spotty. From this point, we can use the changing pattern to calibrate the growth rate of lattice-mismatch material. In the case of InAs on GaAs, the critical thickness is 1.7 ML at 450 ºC, growth rate can be calculated by record the deposition time which is use for changing streaky to spotty pattern. The RHEED pattern of InAs growth is also shown on Figure 3.7.

3.3 Atomic Force Microscope (AFM)

The atomic force microscope (AFM) is a very high resolution microscope, with demonstrated resolution of fractions of a nanometer. The schematic representation of AFM system is shown in Figure 3.8. The AFM consists of a microscale cantilever with a sharp tip at its end, typically composed of silicon or silicon nitride with the size in the order of nanometers. When the tip is brought into close proximity of a sample surface, forces between the tip and sample lead to a deflection of the cantilever. Typically, the deflection is monitored by a laser spot reflection from the top of the cantilever into an array of photodiodes. The AFM consists of three mode measurement i.e. contact mode, non-contact mode and tapping mode. The schematic setup of AFM measuring modes are shown in Figure 3.9.

In this work, the AFM images are performed by using SEIKO SPA 400-AFM. The AFM is operated in the tapping mode in order to reduce the friction during the measurement. The scan rate is about 1-2 Hz and the scan size is usually 2×2- 5×5 μm^2 with 512 data points per line scan.

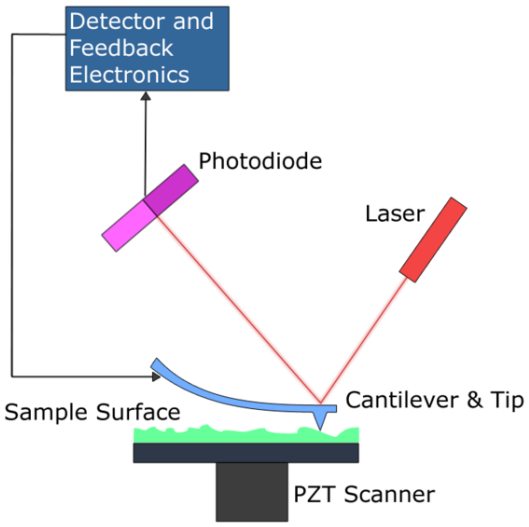

Figure 3.8 Schematic drawing of Atomic Force Microscopy.

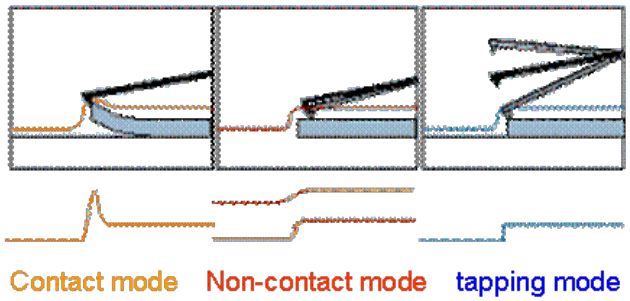

Figure 3.9 The schematic representation of AFM measuring modes including contact mode, non-contact mode and tapping mode. In this work, the AFM is operated in the tapping mode to reduce the friction when measuring.

3.4 Photoluminescence (PL) Measurement

Photoluminescence (PL) spectroscopy is a tool to characterize the optical properties of the samples in this work. The samples are excited by a 488-nm line of an Ar^{+} laser or the 675-nm line of a laser diode. A schematic of the PL experimental setup is shown in Figure 3.10. The laser beam was focused on sample by focal lens. Then, the light signal is chopped before entrance to monochromator and detected by InGaAs

detector and photo multiplier tube. A high-pass filter is used to filter the visible-light noise and the reflected laser beam signal. A chopper and the lock-in amplifier are used to enhance the signal and increase the signal ratio by the standard lock-in technique.

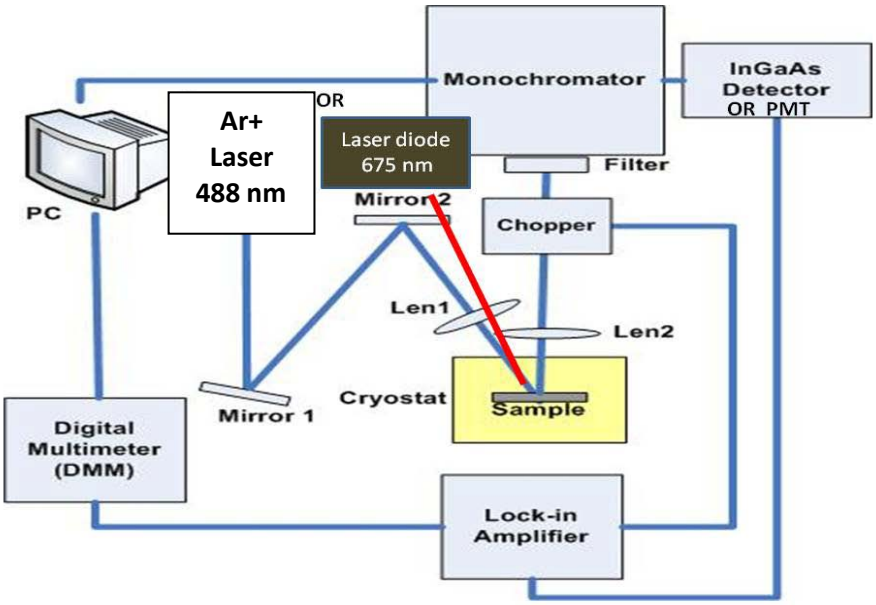

Figure 3.10 Schematic of the PL experimental setup

An example, the interpretation of PL data can simply be described as shown in Figure 3.11 and Figure 3.12. In case of nanostructures with different size in Figure 3.11, the ground state PL peak energy contains information about the size of the nanostructure. When increase of nanostructure size, it is resultted in a lower quantized energy levels of both holes and electrons, which causes a lower energy peak position. Therefore, the peak position can be used to relatively compare the size of nanostructure.

For the shape of PL spectrum from nanostructure array (Figure 3.12), there exists broadening of the spectrum. This broadening, which is measured in terms of a full width at half maximum (FWHM) or PL linewidth, is related to the nanostructure size distribution.

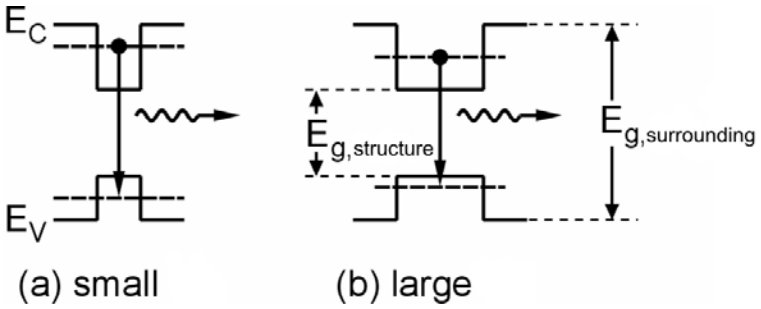

Figure 3.11 Simple interpretation of the PL data obtained from a nanostructure. In case of small-size nanostructure (a) the PL peak energy position is higher compared with large-size nanostructure (b) [52].

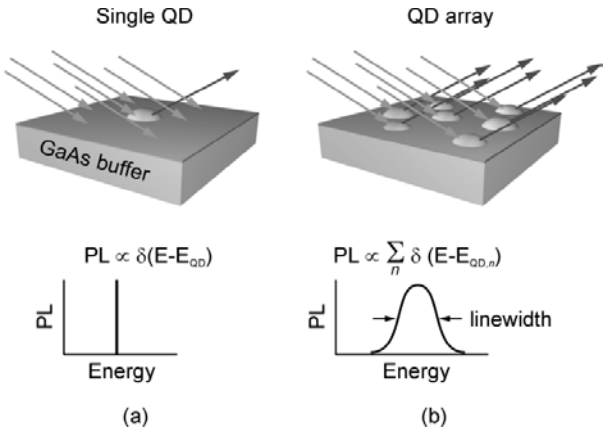

Figure 3.12 Simple interpretation of the PL spectrum obtained from the nanostructure. In (a) the PL spectrum is very narrow due to the delta-function like density of states; and in (b) the average size corresponds to the PL *peak* energy position and the PL linewidth corresponds to the *size distribution* of the array [52].

3.5 Spectral Response Measurement

The spectral response measurement is another method to characterize optical properties of the samples in this work. The samples are used as detector for detecting selected-wavelength light from monochromator. A schematic of the spectral response experimental setup is shown in Figure 3.13 The white light is chopped before entrance

to monochromator and detected by sample. A chopper and the lock-in amplifier are used to enhance the signal by the standard lock-in technique.

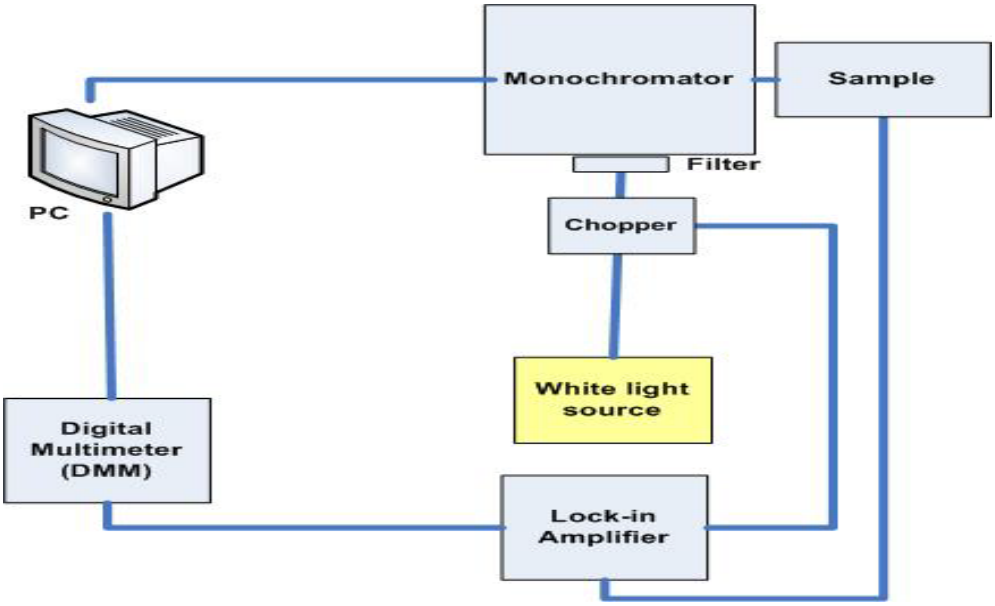

Figure 3.13 Schematic of the Spectral response experimental setup

3.6 Metallization process

In this dissertation, metallization process is prepared for electrical (I-V) characterization and spectral response measurement. Alcatel filament metal evaporator system is used for electrode forming. AuZn alloy is used as ohmic contact of p-GaAs while AuGe/Ni alloy is used as ohmic contact of n-type GaAs. Au is also used for Schottky contact. The metallization process is started by evaporating the AuZn alloy on p-GaAs. After the sample is removed from the evaporator, it is annealed at 490°C for 5 minute under forming gas flow. Then, the AuGe/Ni alloy is coated on n-GaAs and is annealed at 450°C for 2 minute and 30 second under the same ambient.

Figure 3.14 Filament metal evaporator.

3.7 Experimental Procedures

All Samples were fabricated by RIBER 32P conventional solid-source molecular beam epitaxy system. Semi-insulator, n-type, and p-type (100) GaAs substrates were used as the starting substrate. In this thesis was analyzed the properties HD-QDMs, and QRs were inserted in solar cell structure.

The first series was found the optimal stack number of HD-QDM by measuring photocurrent density. The number of stack was varied from 1 to 3, 5, 7 and 10 stacks. In this series, n-type GaAs substrates were used as starting substrates. Before HD-QDMs growth, native oxide of GaAs surface was removed from substrates by ramp the substrates temperature to 600°C under As_4 flux at beam equivalent pressure (BEP) of 8×10^{-6} Torr until the reflection high-energy electron diffraction (RHEED) showed streaky patterns. Then, 400 nm GaAs buffer layer was grown on a substrate at 580°C. Then, 1.8 ML of InAs was deposited at a lower growth temperature of 500°C and lower growth rate of 0.01 ML/s. Next, the thin-capping-and-regrowth technique was used for 5 cycles to create HD-QDM. The stack in this series was separated by 40 nm GaAs spacer. Then,

the optimal stack of HD-QDM was used to characterize and analyze the optical properties and the electrical properties.

In another series, QR structures were integrated into solar cell structure. The details of investigation are as follow. The first batch of samples is prepared on (001) semi-insulator (SI) GaAs substrates. The growth process starts from growing a 300 nm thick GaAs buffer layer by conventional MBE technique at 580°C. The substrate temperature is decreased to 350°C for migration enhanced epitaxy (MEE) of a 50 nm thick $Al_{0.3}Ga_{0.7}As$ barrier layer. Then, the As_4 flux is shut off and the substrate temperature is further decreased from 350 to 300 and 250°C for Ga droplet depositions. Ga flux is controlled with equivalent to GaAs growth rate of 0.5 ML/s. Ga droplets with of 3, 5 and 7 ML were used in this studied. After droplet deposition, the crystallization process starts at of 200°C under As_4 pressure of 8×10^{-6} Torr. GaAs QRs are created from Ga droplets. After this step, the optimal structure of QR was chosen to growth InGaAs QR with low In content. Finally, InGaAs QR was used to characterize and analyze the optical properties and electrical properties.

CHAPTER IV

HIGH DENSITY QUANTUM DOT MOLECULE INSERTION LAYER IN PHOTOVOLTIC STRUCTURE

This chapter shows the experimental results and discussions from HD-QDM structure. The surface morphology of HD-QDMs is examined by AFM. The stacking number of HD-QDMs is varied from 1 to 10 to search for the optimum stack number. PL and spectral response measurements are used to analyze optical properties of HD-QDM structures compared with the conventional QD structure. I-V characterization is used to confirm and analyze electrical properties from HD-QDM structures compared with the conventional QD structure as well as with a non-QD reference cell.

4.1 Surface morphology of HD-QDM

The surface morphology of all samples was observed by tapping mode AFM. HD-QDM and QD structures were characterized and compared. Figure 4.1 shows AFM images and cross-sectional profiles of 1-stack HD-QDMs and those of 1-stack QDs. The density of QDs in the QD sample is equal to 2.8×10^{9} cm^{-2}, while the QD density of HD-QDMs is about 1.8×10^{10} cm^{-2}. The difference in dot size-uniformity could be observed from the AFM images in Figure 4.1(a) and 4.1(b) which is also confirmed by the histogram showing dot height distributions in Figure 4.2(a) and 4.2(b) respectively. The average height of QDs is 10.9 nm while the average height of HD-QDMs is 3.65 nm. The standard deviation (S.D.) of QDs is 0.75 while the S.D. of HD-QDMs is 1.33.

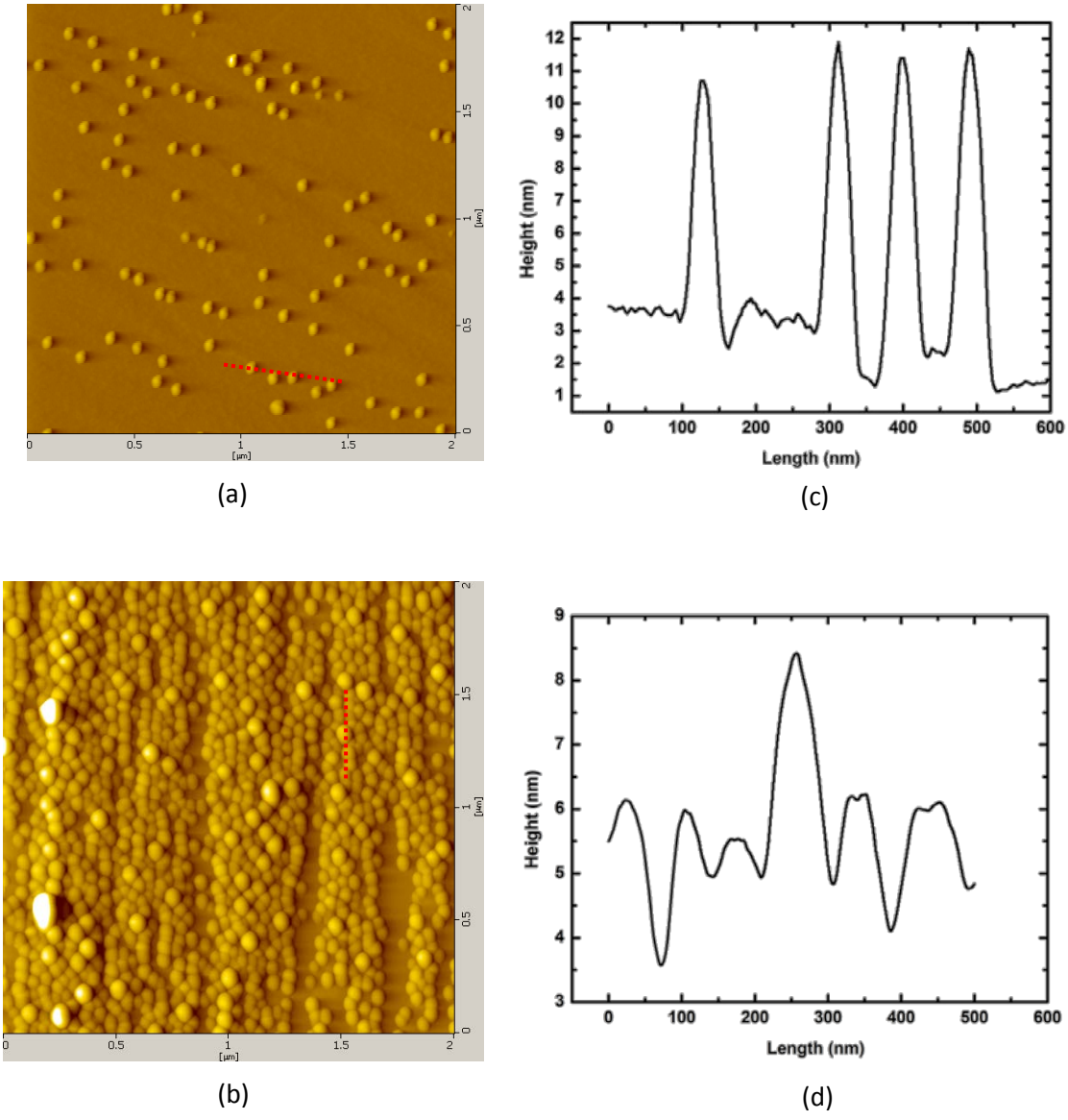

Figure 4.1 2×2 μm^2 AFM images of (a) conventional QDs (b) HD-QDMs. and cross-sectional profiles of (c) conventional QDs (d) HD-QDMs.

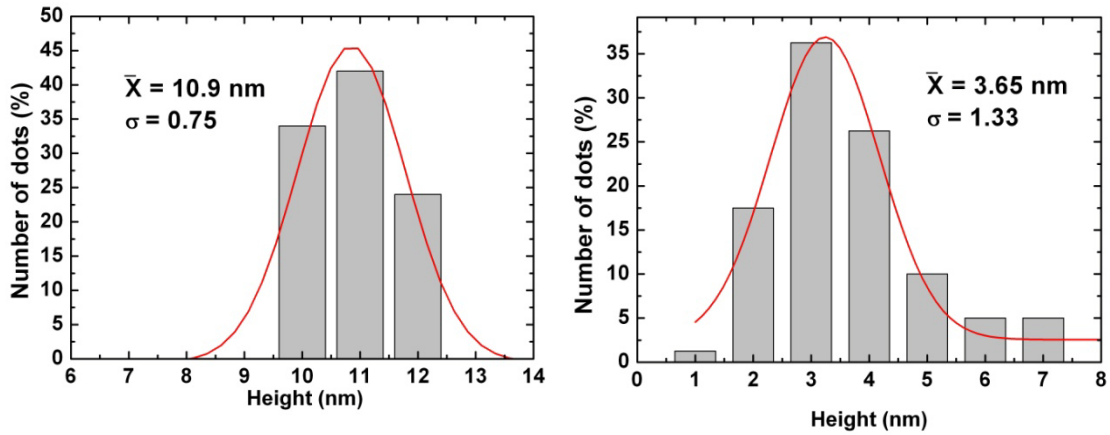

(a) (b)

Figure 4.2 Histogram of height distributions of (a) conventional QDs (b) HD-QDMs.

4.2 Optimum stacking number

An experimental study on the effect of stack number of HD-QDMs was done by measuring I-V characteristic. Five samples having 1, 3, 5, 7 and 10 stacks of HD-QDMs were prepared. After the growth was completed, Schottky and Ohmic contacts were formed on the samples for photocurrent density measurement under the standard AM1 (100 mW/cm^2) light source. The exposure area of samples was approximately 6 mm^2. Figure 4.3 shows the experimental result of photocurrent measurements of all Schottky HD-QDM samples under AM1 illumination. All samples were reverse biased and thus operated in the photo-detection mode. The photocurrent densities under reverse bias of 1 V were plotted and compared among the five samples having 1, 3, 5, 7 and 10 stacks of HD-QDMs. The current density is increased when the stack number increases from 1 to 5, reflecting the larger effective volume of QDMs. However, when the stack number exceeds 5, the photo-current density drops and for the thickest sample with 10 stacks of QDMs, the photo-current density is even worse than that of the1-stacked sample. This is possibly due to degraded QDMs quality when too many stacks of HD-QDMs are

presented. Therefore, 3 to 5 stacks of HD-QDMs are the optimum range and suitable for our QDM bulk solar cell structure.

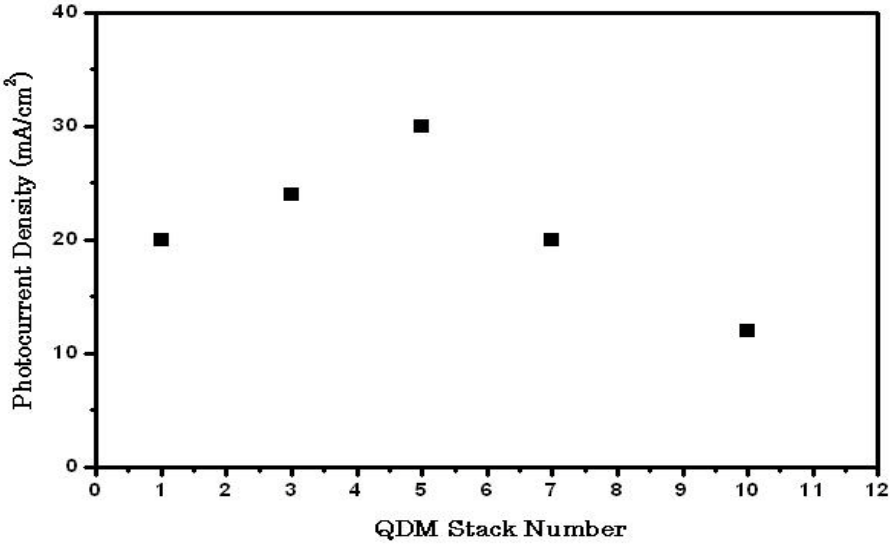

Figure 4.3 Photocurrent density as a function of the number of HD-QDM stacks in the HD-QDM Schottky-junction solar cell structures.

4.3 Photoluminescence (PL) measurement

In this experiment, we choose the best structure to characterize and analyze the optical properties by PL measurement. From engineering point of view, we choose 3-stack HD-QDM structure for measuring PL, and we compare this result with a 15-stack conventional QD structure. The chosen 3-stack HD-QDMs in this comparison with 15-stack QDs since the process in HD-QDM preparation is done by five cycles of the thin-capping-and-regrowth process for each stack. Therefore, the total cycles of 3-stack HD-QDMs are 15 cycles.

Figure 4.4 shows the PL spectrum of a 3-stack HD-QDM and a 15-stack QD samples at 20 K. The PL intensities between HD-QDMs and conventional QDs under the same condition of PL setting and temperature, HD-QDMs provide stronger PL signals than conventional QDs. This behavior reflects a higher dot density grown on a fewer

stack number by the novel growth technique of thin-capping-and-regrowth MBE process.

In a comparison of the PL peak, the PL peaks of HD-QDMs are at around 1.15 eV which is higher energy than those of QDs at around 1.05 eV. This difference in the energy of the PL peaks of the two samples originates from the respective quantized energy levels of different QD sizes. Dot uniformities in HD-QDM and QD samples are again reflected by the FWHM values of the PL peaks. The uniform dot size of the 15-stack QD sample gives a narrower FWHM of 40 meV. The modified MBE process of growing the 3-stack HD-QDM sample gives a higher dot density per stack but less dot uniformity. This leads to broader PL peaks with FWHM of 70 meV.

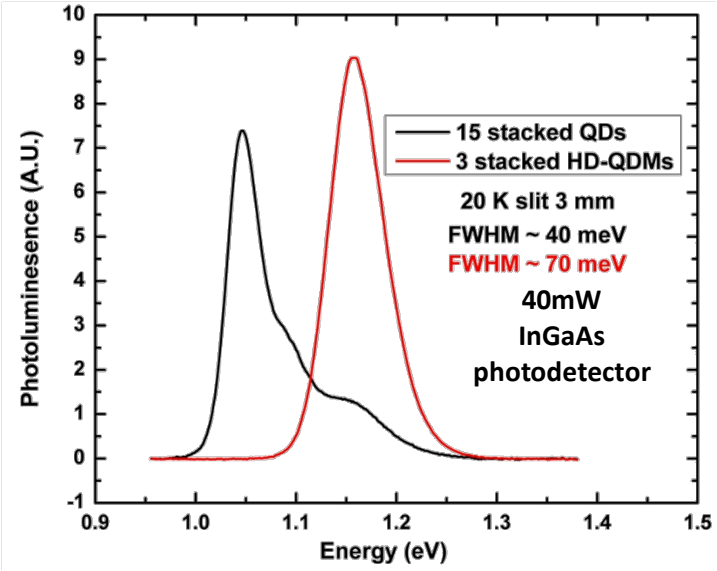

Figure 4.4 Photoluminescence of 15-stack QDs and 3-stack HD-QDMs at 20 K.

Temperature dependent PL measurements are shown in Figure 4.5. The PL peaks of both samples are red-shifted when the measurement temperature is increased. The dependence follows the Varshni equation [60]. The PL spectrum of the QD sample at low temperature shows several peaks of the ground and excited states. At high temperature, only the narrow PL peak from the ground state is observed. On the contrary, the PL peaks of HD-QDMs remain broad and unchanged in Gaussian shape at all temperatures. The FWHM of the PL peak of the 15-stack QDs is more sensitive to

temperature due to several dominant dot sizes. For the multi-stack QD sample, the dot size in each stack has a tendency to be larger [61]. This variation in dot size is also found in the 15-stack QD sample leading to temperature sensitivity of FWHM and confirmed by the result of power dependent PL as shown in Figure 4.6.

The PL spectrum of the 15-stack QDs is quenched in the high energy side, while the PL spectrum of the 3-stack HD-QDMs is quite stable at high temperature. This phenomenon could be explained by the thermal activation of carrier from QDs to the GaAs matrix. In contrast, the PL peaks of the HD-QDMs remain broad and unchanged in Gaussian shape at all temperatures. This temperature insensitivity of HD-QDMs is due to close-packing of QDs so that carriers could relax to nearby QDs having different dot sizes.

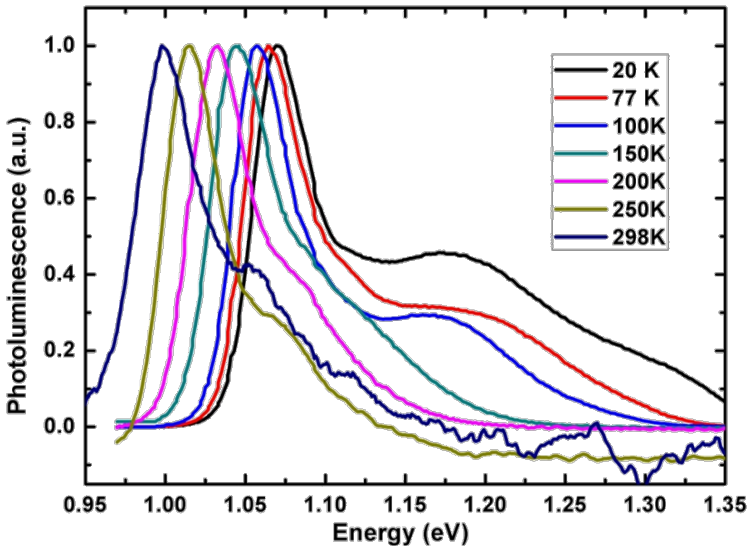

(a)

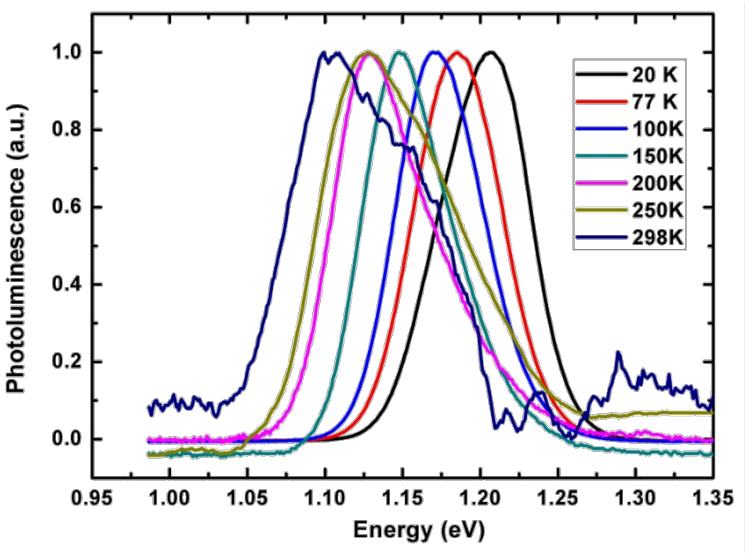

(b)

Figure 4.5 Normalized Photoluminescence of (a) 15-stack QDs and (b) 3-stack HD-QDMs at temperature ranging from 20 K-298 K.

The power excitation dependence of the PL of the 3-stack HD-QDMs and the 15-stack QDs are shown in Figure 4.6 (a) and (b) respectively. In Figure 4.6 (a), the PL spectrum of the 15-stack QDs is different from Figure 4.5 (a) with the same power and temperature. We believe that the difference in the PL shape is attributed to the position of optical pumping on the sample surface. However, both PL results from Figure 4.5 (a) and 4.6 (a) are taken from the same position on the sample surface. With increasing the power excitation, we find that both structures have similar trend. The PL spectra exhibit no significant changes with the excitation power; this feature can be explained by considering that the carriers are populated randomly into the QD states at low temperature [62]. We presume that in the 15-stack QD sample, the residual strain from the lower QD stacks can introduce earlier creation of larger dots. Therefore, the PL of the 15-stack QD sample seems to be composed of three different QD sizes. In the 3-stack HD-QDM structure, all QDMs are composed of similar dot size. Nevertheless, dominant dot uniformity in the 3-stack HD-QDM structure is poorer than the 15-stack QD

structure. This fact is confirmed by broader FWHM of the 3-stack HD-QDMs and comparing to that of the 15-stack QDs.

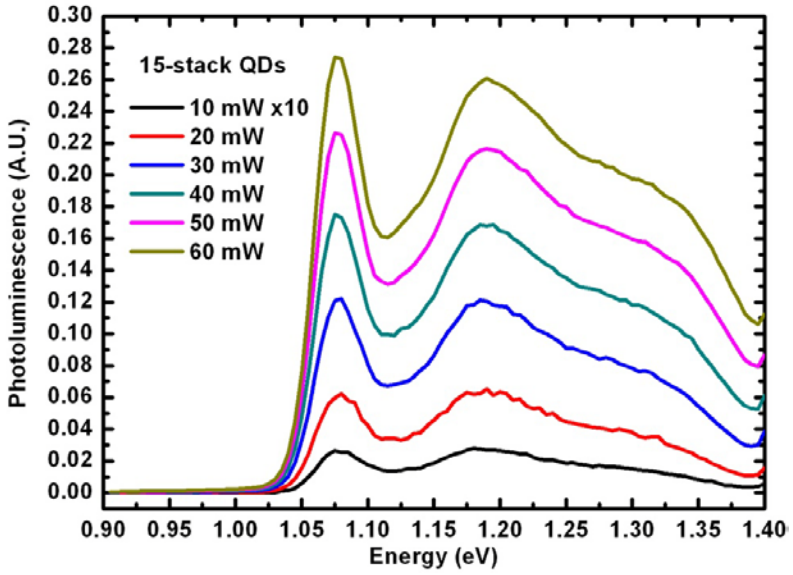

(a)

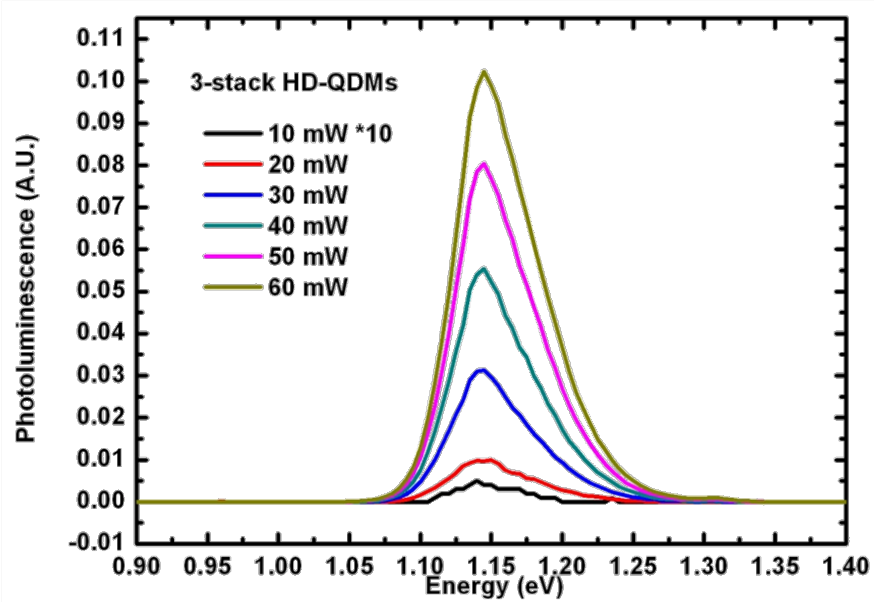

(b)

Figure 4.6 Excitation power dependent PL between 10-60 mW of (a) 15-stack QDs (b) 3-stack HD-QDMs.

4.4 Spectral response measurement

It is found that the spectral response measurement that both spectra of the 3-stack HD-QDM and the 15-stack QD Schottky samples have been extended beyond the band edge of GaAs at 870 nm comparing to the sample without dots, as shown in Figure 4.7. The spectral response peak of the 15-stack QD sample is narrower and centered at 907 nm, while the 3-stack HD-QDM sample provides a broader response peak between 915 and985 nm. The extended peak area from the 15-stack QD sample is less than peak area from the 3-stack HD-QDM sample by about 34 % when compared with the peak area from the GaAs substrate, as shown in Figure 4.7. These broader spectral responses of HD-QDMs are required for high performance of QD solar cells. The uniqueness of HD-QDMs is high density of repeated different dot sizes in one stack. Therefore, the 3-stack HD-QDM sample gives higher sensitivity than the 15-stack QD sample due to higher density in the dot volume in the shallower active nanostructure.

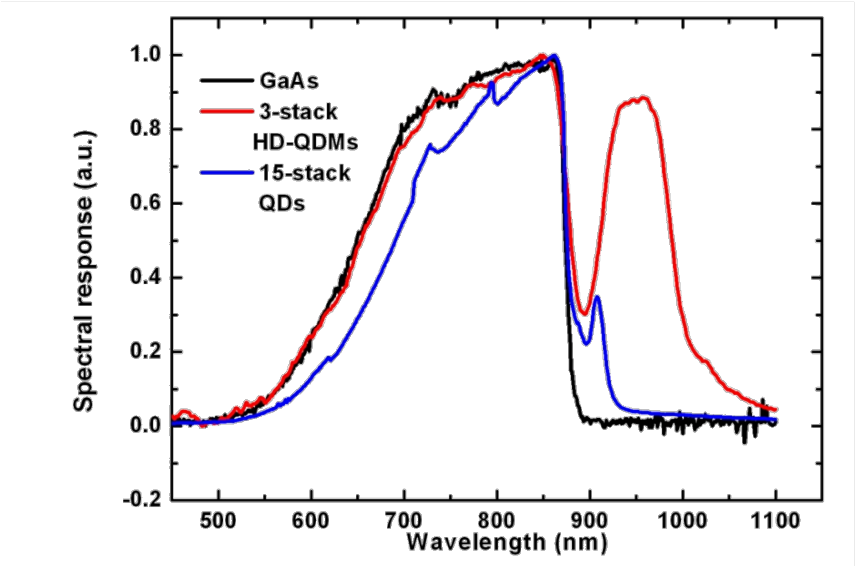

Figure 4.7 Normalized spectral response curves of Schottky-type 3-stack InAs HD-QDM and 15-stack InAs QD solar cells comparing to Schottky GaAs solar cell without dots.

When the light intensity is increased from 1 to 1.5, 2.0, 2.5 and 3.0 suns, the extended spectrum beyond band edge of GaAs from both 15-stack QD sample and 3-stack HD-QDM sample are observed. The extended area spectrum of the 15-stack QD sample varies from 8.8 % to 7.9 %. On the other hand, the extended area spectrum of HD-QDM sample is from 42. % to 35.2 %. It implies that the QD sample has better crystal quality than that of HD-QDM sample due to growth at higher temperature of QDs. However, the HD-QDM sample is more sensitive than the QD sample due to its higher dot density as seen in Figure. 4.8.

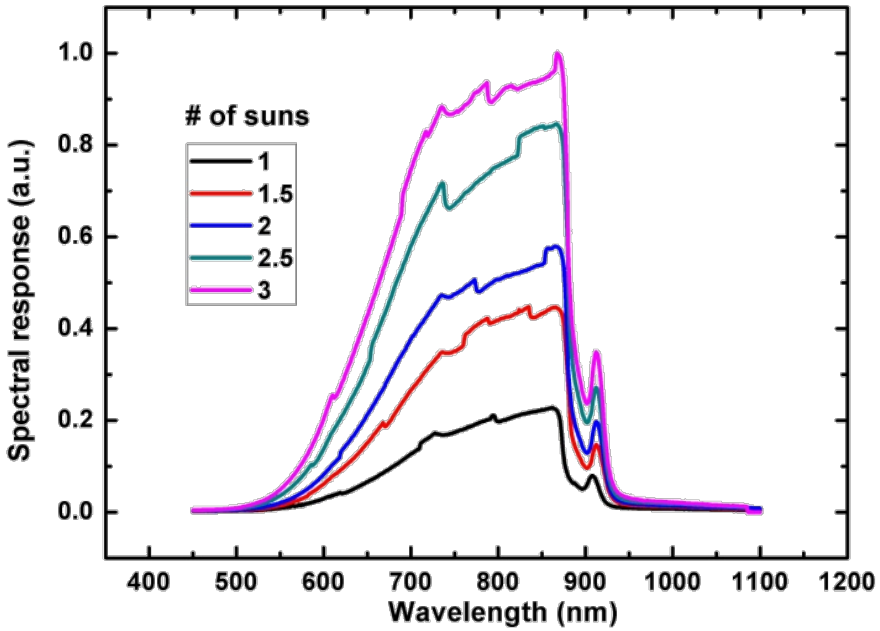

(a)

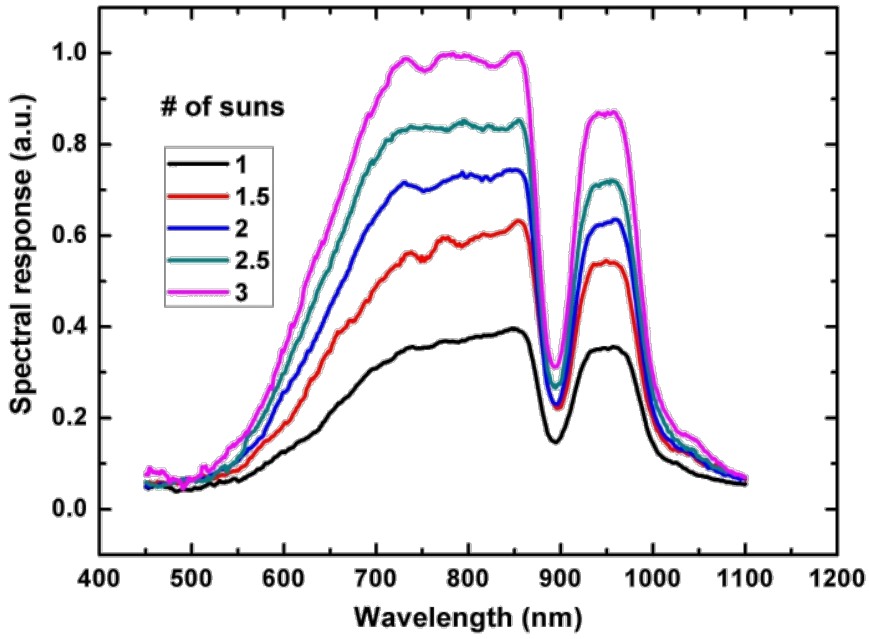

(b)

Figure 4.8 Spectral response curves of (a) Schottky- type 15-stack InAs QD and (b) 3-stack InAs HD-QDM solar cell under concentrated light source.

4.5 I-V Characterization

The electrical properties (I-V characteristic) are measured by a curve tracer Textronic model 177 and a solar simulator Kratus model LPS255S. Figure 4.9 shows I-V curves of a P-I-N reference sample with varying light intensity. It is found that $V_{cut\text{-}in}$ of the reference cell is 1.1 V. When the light illuminats at 1 sun with AM 1 intensity, the reference cell gives $V_{oc} \sim 0.6$ V and $J_{sc} \sim 8.19$ mA/cm^2. When the light intensity is increased from 1 to 2, 3, and 4 suns, the photocurrent does not increase linearly with increasing light intensity. The I-V curves indicate poor fill factor and dropping V_{oc} compared with the $V_{cut\text{-}in}$. This might be a non-optimum design in the GaAs/AlGaAs hetero-junction which would produce a notch in the energy band diagram of hetero-junction. This notch can block the current flow [63]. Therefore, the solar cell design has to be improved. Moreover, it is shown that R_s of the structure is pretty high. This cause is from the fact that the junction depth of p-n is not appropriate [63].

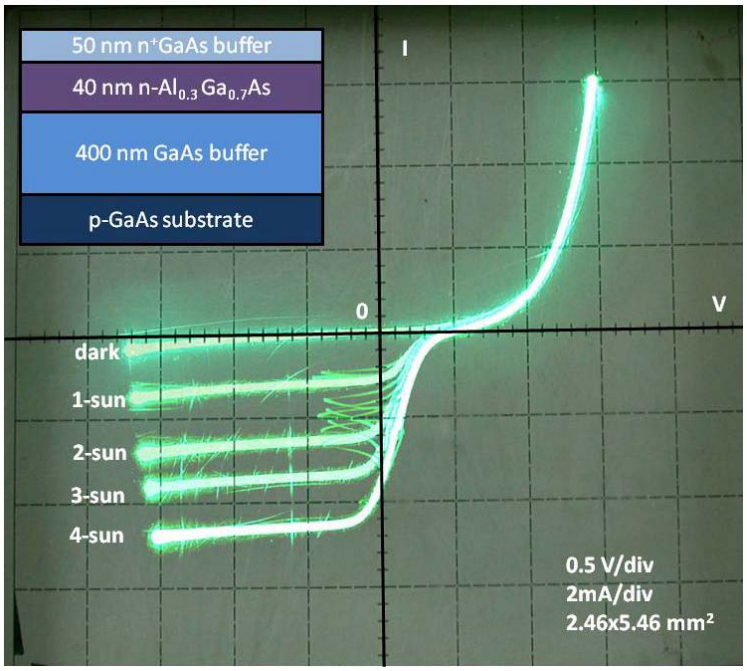

Figure 4.9 I-V curves of GaAs/AlGaAs reference sample with dark condition and 1-4 suns light intensity.

Figure 4.10 shows I-V curves of the 15-stack QD sample. The $V_{cut\text{-}in}$ is 0.68V. Under 1 sun intensity, the 15-stack QD sample also gives V_{oc} ~ 0.6 V and J_{sc} ~ 7.89 mA/cm^2. It has some drop in J_{sc} when compared with the reference sample. However, when the light intensity is increased, the 15-stack QD gives more current density than the reference sample. This extra photo-current could be from the extended spectral response of the QD structure as seen in the spectral response result.

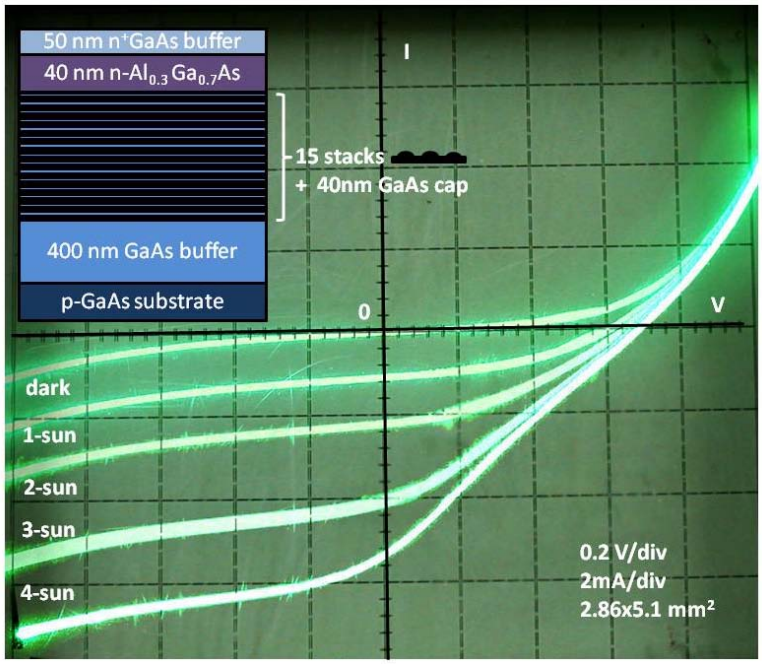

Figure 4.10 I-V curves of 15-stack QD sample with dark condition and 1-4 suns light intensity.

I-V curves of the 3-stack HD-QDM sample is shown in Figure 4.11. The $V_{cut\text{-}in}$ of the sample is 0.66V. In an I-V characteristic comparison between the 3-stack HD-QDMs and 15-stack QDs samples, it is found that R_s of the 3-stack HD-QDMs is higher than R_s of the 15-stack QDs. When the light illuminats at the 1 sun intensity, V_{oc} of the HD-QDM cell is dropping to ~0.4 V and gives J_{sc} ~ 7.64 mA/cm^2. From the highest R_s of this structure when compared with other samples, it might be a cause that the current density and V_{oc} of the 3-stack HD-QDM sample are not improved. Even in the concentrated light condition, this structure does not given extra photocurrent like in the 15-stack QD case.

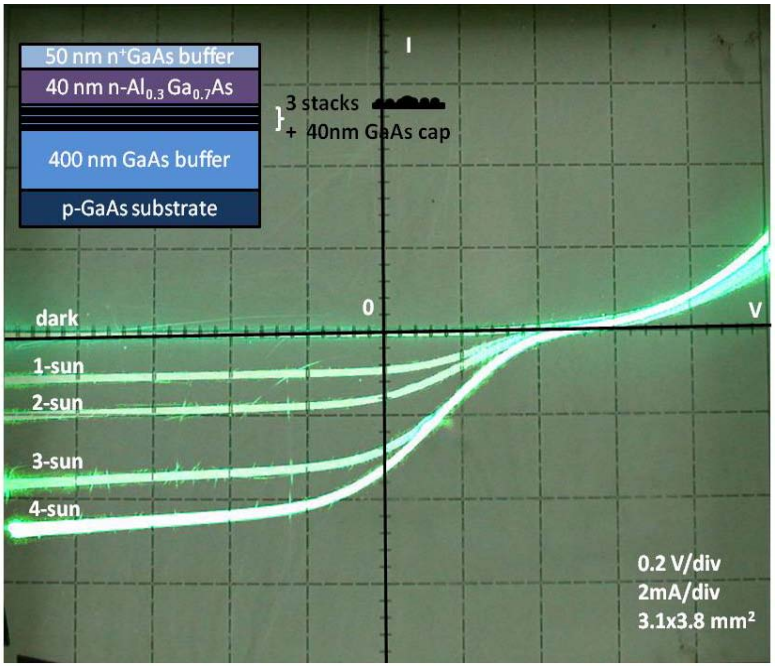

Figure 4.11 I-V curves of 3-stack HD-QDM sample with dark condition and 1-4 suns light intensity.

In this chapter, the AFM images of HD-QDM and QD samples are shown and compared. Optimization of the stack number of HD-QDM is done. A 3-stack HD-QDM structure is compared with a 15-stack QDs structure. The PL result of the 3-stack HD-QDM gives higher spectral peak and larger FWHM than the 15-stack QD sample. The spectral response results show that the 3-stack HD-QDM gives more extended spectral response than the 15-stack QD. I-V characteristic results indicate that the solar cell structure has to be improved by a proper design. The current density of the 15-stack QD sample is the highest under high concentration light from this experiment. However, this still cannot be concluded that QD structure gives better results because there are many factors such as the total thickness of the cell, doping concentration, etc., that have to be investiagted.

CHAPTER V

QUANTUM RING INSERTION LAYER IN PHOTOVOLTIC STRUCTURE

This chapter reports on the insertion of QR nanostructure, which is fabricated by droplet epitaxy (DE) technique, into a solar cell structure. The effects of droplet forming temperature and Ga amount on the structure of GaAs QRs are studied. InGa droplets with In content of 0.1 are also used in QR fabrication. 1- and 5-stack InGaAs QR samples are prepared for PL measurement and spectral response measurement to analyze optical properties from QR samples. I-V characterization is used to confirm and analyze electrical properties from QR structure compare with non-QR reference cell.

5.1 Surface morphology of Quantum Ring

5.1.1 GaAs/AlGaAs Quantum Ring

The effect of forming conditions of GaAs ring and double-ring shape nanostructures are observed in this work. It is found that at most of deposition temperatures for small droplets, GaAs single quantum rings (QRs) are formed on an AlGaAs surface. However, the droplets with an amount of 7 ML Ga and droplet forming temperature of 350°C are transformed to double quantum rings (DQRs) as being displayed in the AFM image at the lowest-right corner of Figure 5.1. Due to the high volume of 7 ML droplets deposited at 350°C and As_4 pressure at 8×10^{-6} Torr, the As atoms are not sufficient to form QDs, and the migration of excess Ga atoms from the center of droplet is higher than other cases during the crystallization process. These two reasons lead to the formation of DQRs having outer and inner rings as reported by Mano *et al*. [32, 64]. It is also observable from Figure 5.2 that both of typical GaAs single QR and DQR are asymmetry. The cross sectional profiles along [110] show larger ring lobes than those along [1-10]. This is due to the anisotropic behavior of Ga atom migration during the crystallization of Ga nanodroplets.

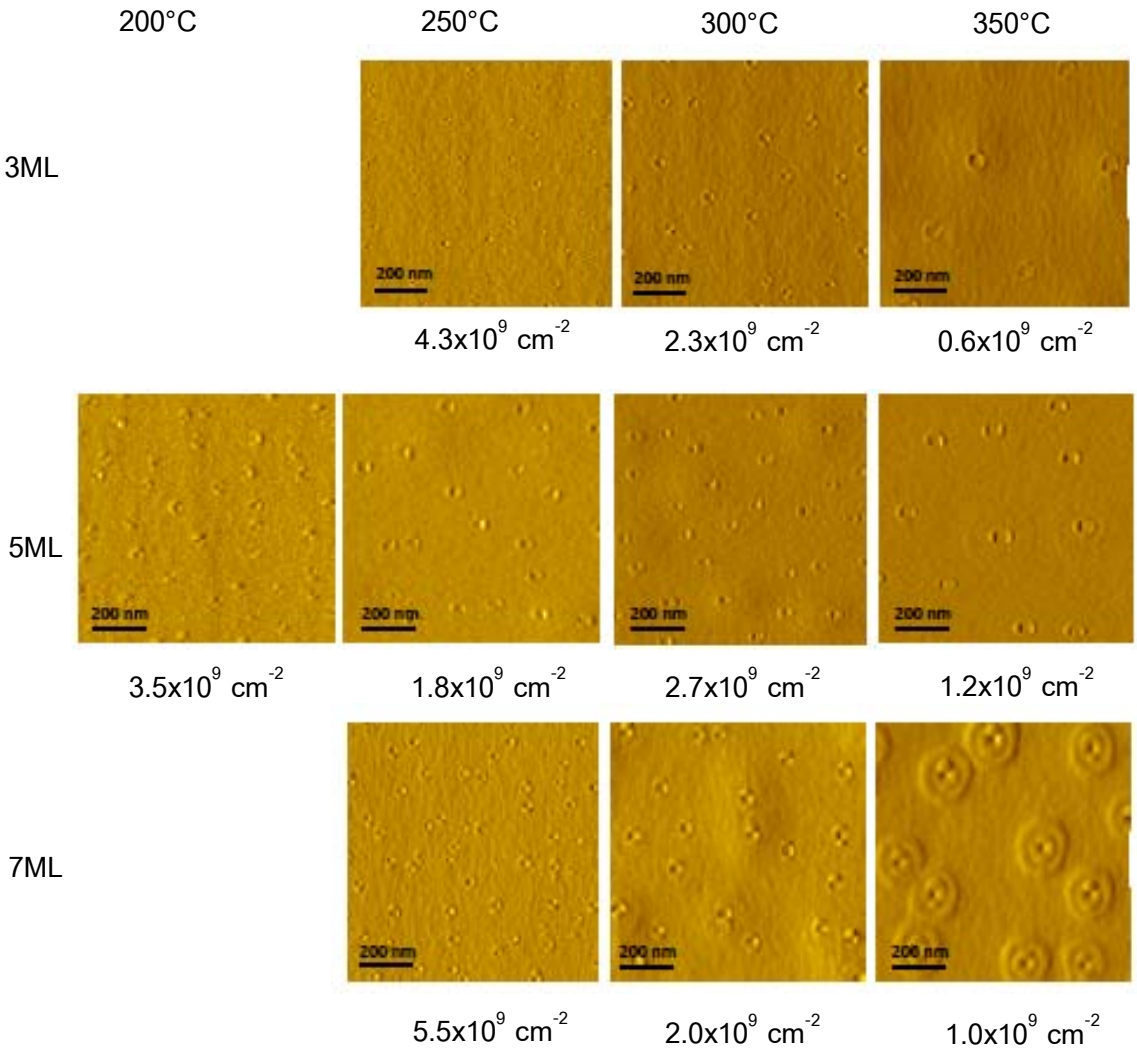

Figure 5.1 1×1 μm^2 AFM images of GaAs quantum rings grown by DE with crystallization temperature of 200°C at with different growth conditions, i.e. droplet thicknesses (3, 5, 7 ML) and droplet forming temperatures (250, 300, 350°C).

Figures 5.3(a) and (b) show the QR density changing with droplet forming temperature and droplet deposition amount. When the droplet forming temperature is high, the small droplets are merged into larger droplets. This causes to lower the density of QRs at most of high deposition temperatures in all cases of droplet amounts as shown in Figure 5.3(a). It is, therefore, recommended that an optimal condition of low droplet

forming temperature of 250°C and 7ML droplet amount can give high QR density as well as uniform ring dimension which are suitable for QR solar cell application. However, the trend is different in the case of 250°C during 3-7 ML droplet deposition. This phenomenon can be explained by merging of droplets into a continuous layer leading to reduced density. Then, the newly arrived Ga adatoms form additional droplets above the layer. Therefore, the density of droplets has been renewed [65] as shown in the black line of figure 5.3(b). In the case of 300°C and 350°C droplet forming temperatures, the QR density virtually increases with larger droplet deposition amount. This is a difference in the case of 250°C droplet forming temperature where the droplets are larger and have lower density. Thus, by increasing the Ga amount, more Ga droplets can be formed on the surface due to more adatoms deposited [66].

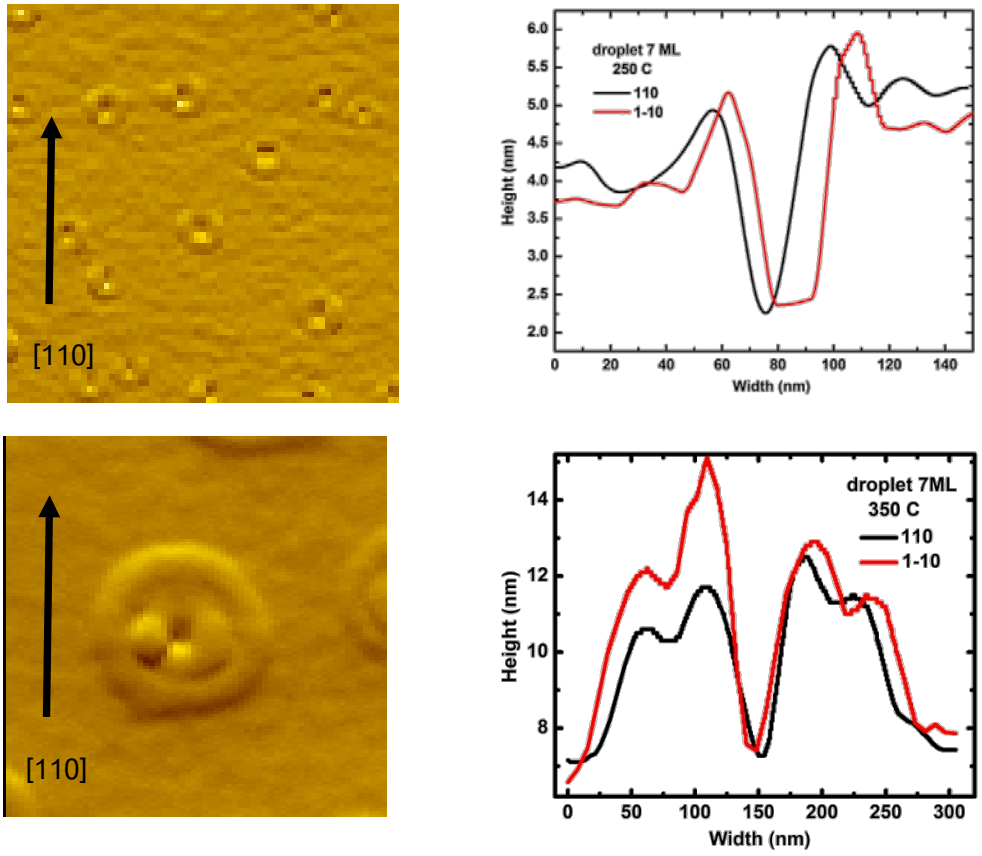

Figure 5.2 Typical GaAs QR, DQR and their cross sectional profiles along [110] and [1-10] crystallographic directions.

The ring size increases at higher droplet forming temperature due to high diffusion ability. However, the QR diameter at the same droplet forming temperature is pretty unchanged with variation in diameter of less than 20% except for the sample grown at 250°C and that of DQR formed at 350°C. The diameter of QRs is in the range of 45 nm to 130 nm. Considering QR height, it is found that there are more variations than the diameter in various growth condition, i.e., different thickness of Ga droplet and different droplet forming temperature. However, the QR height of 5ML conditions is found to be the highest QR height in all droplet forming temperatures, except that of the DQR case. The height of QR is in the range of 0.7 to 1.85 nm. In the case of DQR height, the outer ring height is 3.7 nm while the inner ring height is 2.5 nm.

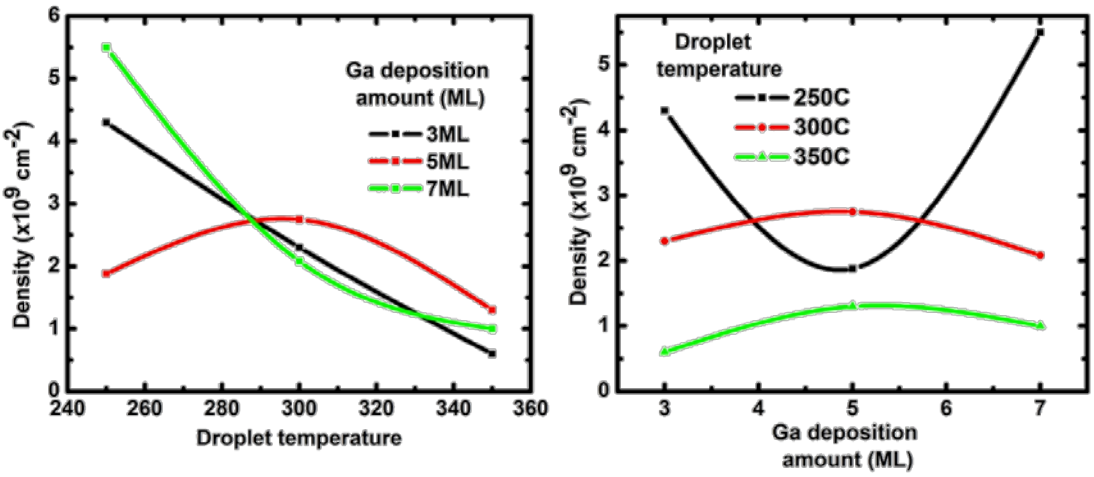

(a) (b)

Figure 5.3 Dependence of quantum ring density on (a) droplet temperature, (b) Ga deposition amount

From the surface morphology of 7 ML GaAs/AlGaAs QR structure, the samples with the droplet-forming temperature of 350ºC and of 250ºC are selected due to the highest size and the largest density, respectively. However, Wu *et al*. (2009) have proposed GaAs/AlGaAs QR to be used for intermediate band solar cell. They reported the PL peak centered at 1.52 eV and showed the spectral response energy range of

1.40–1.77 eV [67]. This extra photo current of spectral response is not observed when compared with AlGaAs/GaAs bulk solar cells. Thus, this dissertation is looking to choose InGaAs/AlGaAs QRs with the same droplet forming condition for intermediate band solar cells aiming at better spectral response at the long wavelength region as well as V_{oc} improvement.

5.1.2 InGaAs/AlGaAs Quantum Ring

InGa droplets with low In content of 0.1 are deposited on an AlGaAs barrier layer with the same droplet forming condition in the Ga droplet process. However, Jevasuwan *et al*. (2010) have reported the influence of crystallization temperature on crystal quality via PL result of InP nanostructures by DE technique. They found that higher crystallization temperatures give higher crystal quality [68]. Moreover, it was reported PL result from InGaAs QRs at crystallization temperature of 250ºC [69]. Thus, the growth conditions of InGaAs QR in this dissertation are droplet forming at 350ºC and 250ºC then crystallization at 250ºC.

The InGaAs nanostructure fabricated by this method has only single ring shape. The transformation from GaAs DQR (in 350ºC droplet temperature and 7.5 ML deposition amount droplet condition) to pure QR shape can be explained by strain relaxation arguments [68]. An AFM image of the InGaAs QRs with deposition forming at 350ºC and crystallization at 250ºC and their cross-sectional profiles of the QRs are displayed in figure 5.4(a) and 5.4 (b), respectively. The average QR height and diameter in the [1-10] direction are ~2.55 nm and ~115 nm. In the [110] direction, the average height and diameter are ~0.8 nm and ~115 nm, respectively. The QR areal density is approximately 1×10^{9} cm^{-2}. In the case of InGaAs QRs with droplet forming at 250ºC and crystallization at 250ºC, the AFM image and cross-sectional profiles of this condition are shown in figure 5.5(a) and 5.5(b). The average QR height and diameter in the [1-10] direction are ~1.61 nm and ~98 nm. In the [110] direction, the height is quite flat. The average height and diameter are ~0.4 nm and ~92 nm, respectively. The QR areal density is approximately 2.6×10^{9} cm^{-2}. As the droplet forming temperature

decrease, it is found that the QR density increase. This is the same direction as the GaAs QR case.

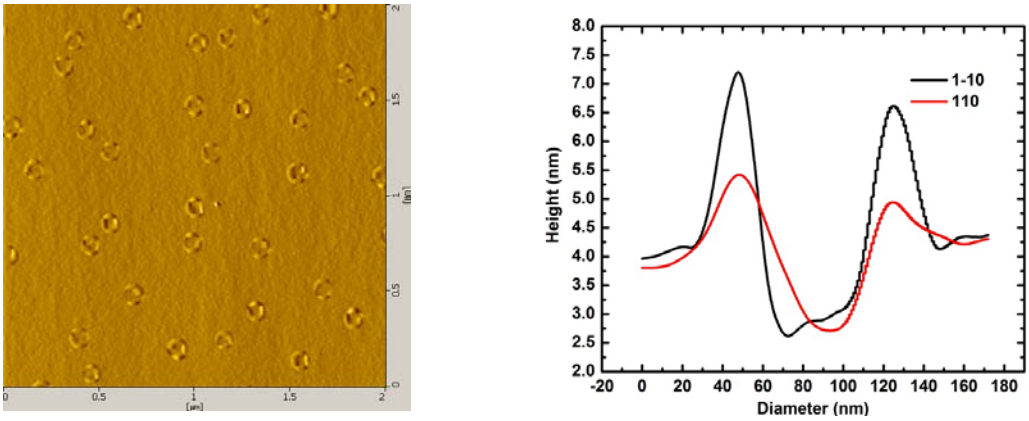

(a) (b)

Figure 5.4 InGaAs QRs grown by DE with 7.5 ML (droplet forming at 350°C and crystallization temperature of 250°C) (a) 2×2 μm^2 AFM images and (b) their cross sectional profiles along [110] and [1-10] crystallographic directions.

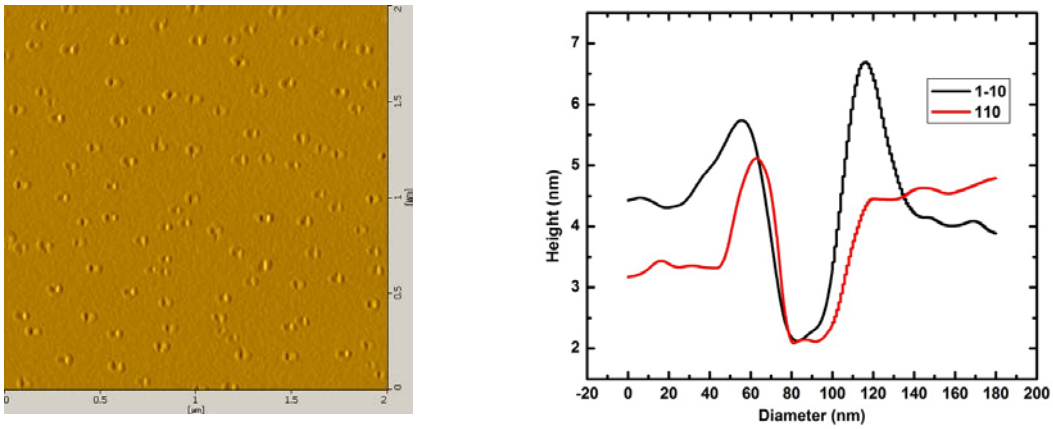

(a) (b)

Figure 5.5 InGaAs QRs grown by DE with 7.5 ML (droplet forming at 250°C and crystallization temperature of 250°C) (a) 2×2 μm^2 AFM images and (b) their cross sectional profiles along [110] and [1-10] crystallographic directions.

5.2 Photoluminescence measurement of InGaAs Quantum Rings

Firstly, single-stack InGaAs QR (droplet forming at 350ºC and crystallization at 250ºC) is selected to characterize and analyze the optical properties via PL. Single-stack InGaAs QRs are grown on 50 nm $Al_{0.3}Ga_{0.7}As$ and capped with the same thickness of $Al_{0.3}Ga_{0.7}As$. Figure 5.6 shows the PL emission from InGaAs QRs at 20 K. The PL peak is centered at 1.35 eV, which has a FWHM of ~85 meV. The PL curve of InGaAs QRs consists of more than one Gaussian curves. Presumably, they are caused by the anisotropic surface-migration of In and Ga atoms during the crystallization process. This phenomenon results in anisotropic shape of such QRs and non-uniform height of QR in different directions.

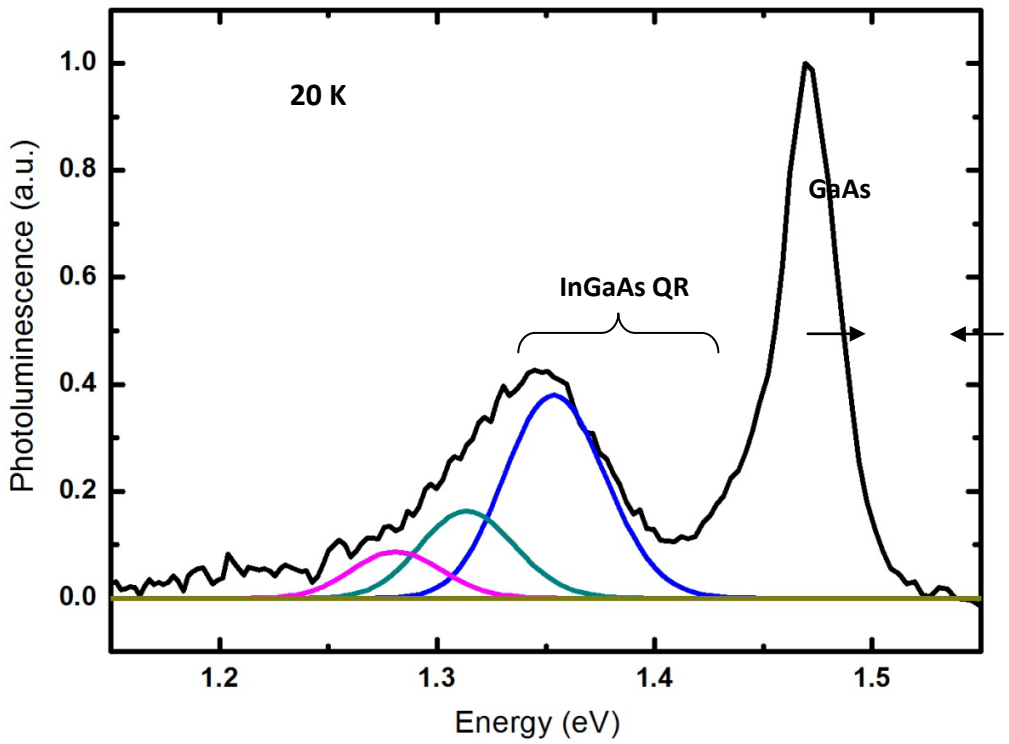

Figure 5.6 Photoluminescence of InGaAs QRs with droplet forming at 350ºC and crystallization at 250ºC

In Figure 5.7, the temperature-dependent PL spectra of 1-stack and 5-stack of InGaAs QRs with an excitation power of 90 mW are shown. The peak intensity of 5-stack is higher than that of single-stack by approximate 4 times. At 20 K, the PL peaks of both InGaAs QR samples are at ~1.35 eV. The FWHM of the 1-stack sample is 85 meV while that of the 5-stack is 100 meV. This result implies that the QR size distribution in the stacked sample is more than that in the non-stacked sample. These FWHMs are the same as in the conventional QD case. With rising temperature, the PL spectrum intensity of the QRs becomes weaker and then hardly detectable. This is due to imperfect crystal quality and the low density of the QRs. The PL from QRs might, however, be improved by changing the crystallization condition or by rapid annealing at high temperature to improve the structural and optical qualities [70-71]. In the case of power dependence PL of 5-stack QRs (droplet forming at 350°C) at 20 K, the PL spectra are unchanged with incident power.

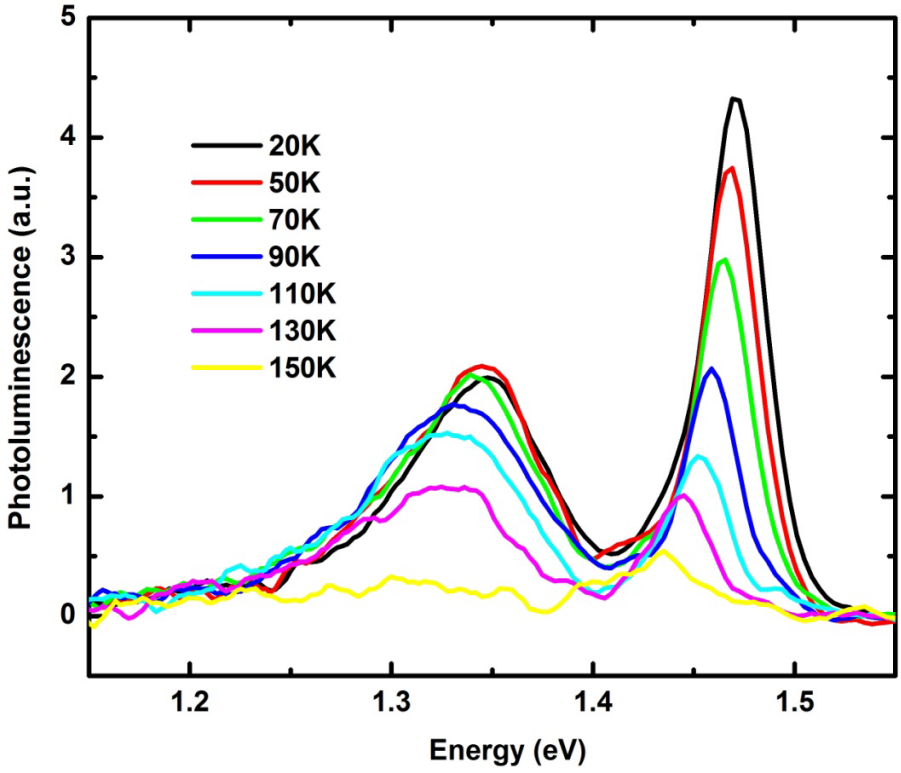

(a)

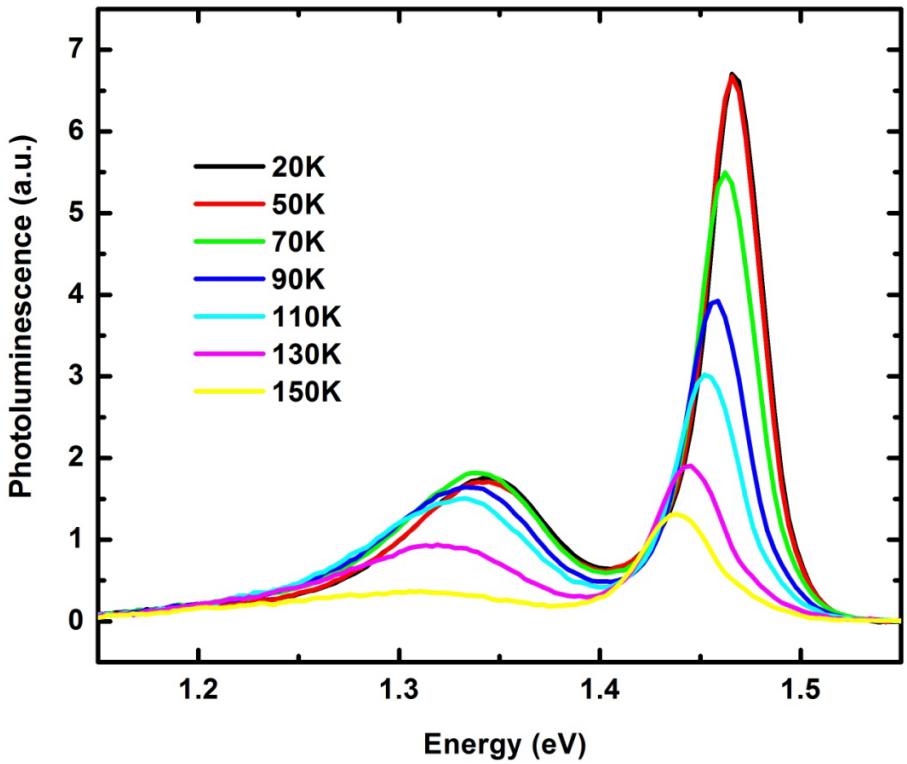

(b)

Figure 5.7 Photoluminescence of (a) single-stack InGaAs QRs and (b) 5-stack InGaAs QRs (droplet forming at 350ºC and crystallization at 250ºC) at temperature ranging from 20 K-150 K.

Figure 5.8 shows the PL spectra of 5-stack InGaAs QRs (droplet forming at 250ºC, crystallization at 250ºC) with an excitation power of 40 mW of 488 nm Ar^{+} laser at 20 K. It is found that the PL of the 5-stack QRs (droplet forming at 250ºC) is merged with GaAs peak. When the PL spectrum is fitted to multiple Gaussian peaks, the PL peak of 5-stack InGaAs QRs (droplet forming at 250ºC) is composed of more than one Gaussian curves. The FWHM of 5-stack InGaAs QRs (droplet forming at 250ºC) is broader than that of 5-stack InGaAs QR (droplet forming at 350ºC). This is due to less uniformity than the 5-stack InGaAs QRs (droplet forming at 250ºC).

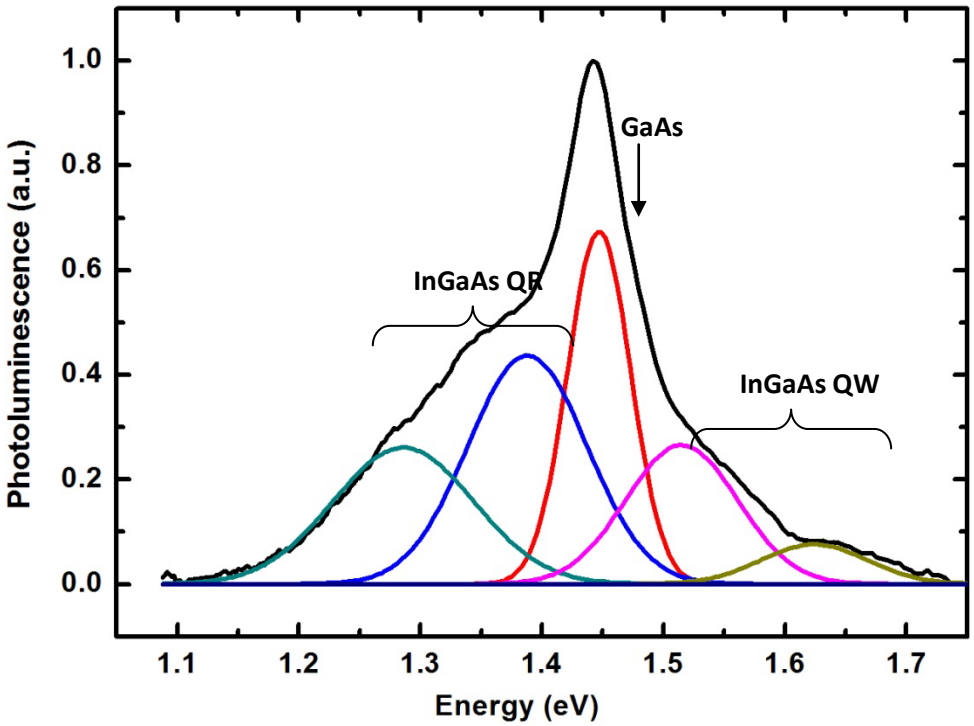

Figure 5.8 Photoluminescence of 5-stack InGaAs QR (droplet forming at 250ºC and crystallization at 250ºC) with an excitation power of 40 mW.

Figure 5.9 shows the temperature-dependent PL of 5-stack QRs (droplet forming at 250ºC) with an excitation power of 40 mW. The temperature-dependent PL exhibits red-shift with increasing temperature, the same results as from the temperature-dependent PL of all other samples. However, the PL of this structure can exhibit higher temperature than the PL of 5-stack QRs (droplet forming at 350ºC). This might be because this structure has a higher density per unit volume than the 5-stack QRs (droplet forming 350ºC). At high temperature region (220-250ºC), it can observe that the PL from QRs is separated from the GaAs peak. The high energy side of QRs might be quenched at high temperature. This also could be explained by thermal activation of carrier from QRs to the AlGaAs.

The excitation-power dependent PL is shown in Figure 5.10. It is found that the PL emission is red-shifted when the power excitation is increased. The FWHM is broad

due to the superposition of the radiation from the GaAs bulk, InGaAs QWs and InGaAs QRs. The simulation extraction results are shown in Figure 5.11. At low power excitation range (20-40mW), the dominant peak stems from GaAs (1.47 eV) and the shoulder peaks originate from InGaAs QWs and InGaAs QRs. When increasing the power excitation, the excited energy peak of the QR is attributed from excited states of QR and become the dominant peak as shown in Figure 5.11. Thus, the maximum peak moves to the low energy side (peak of QRs). The PL from the QRs can overlap with the GaAs peak and can be dominated. Therefore, the PL peak position is red-shifted with rising excitation power as in Figure 5.10.

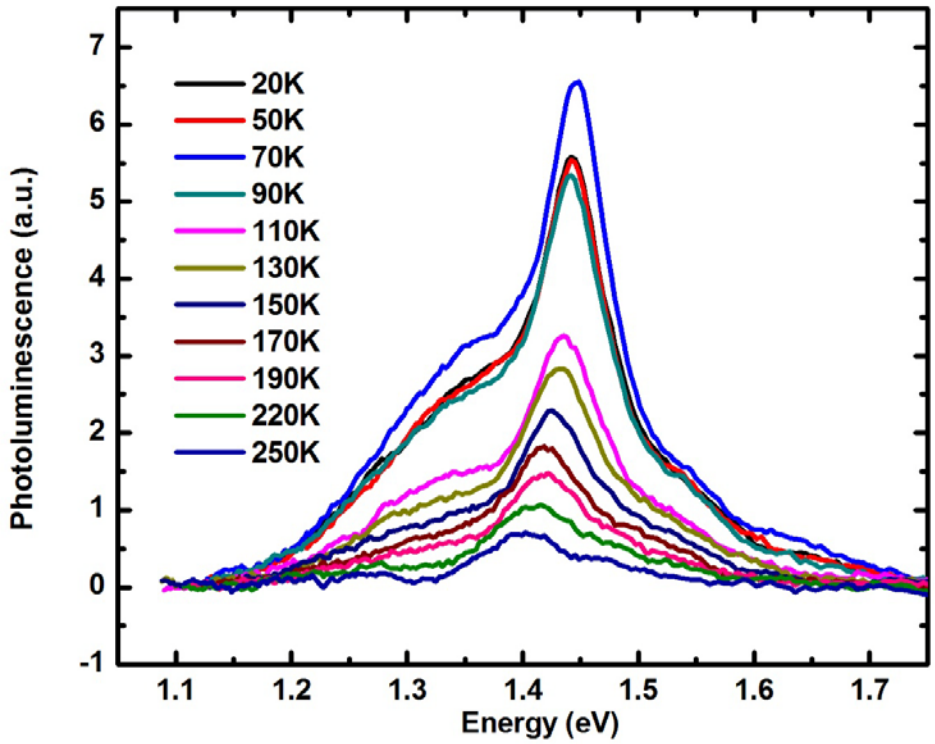

Figure 5.9 Photoluminescence of 5-stack InGaAs QRs with droplet forming at 250ºC and crystallization at 250ºC with temperature ranging from 20 K-250 K.

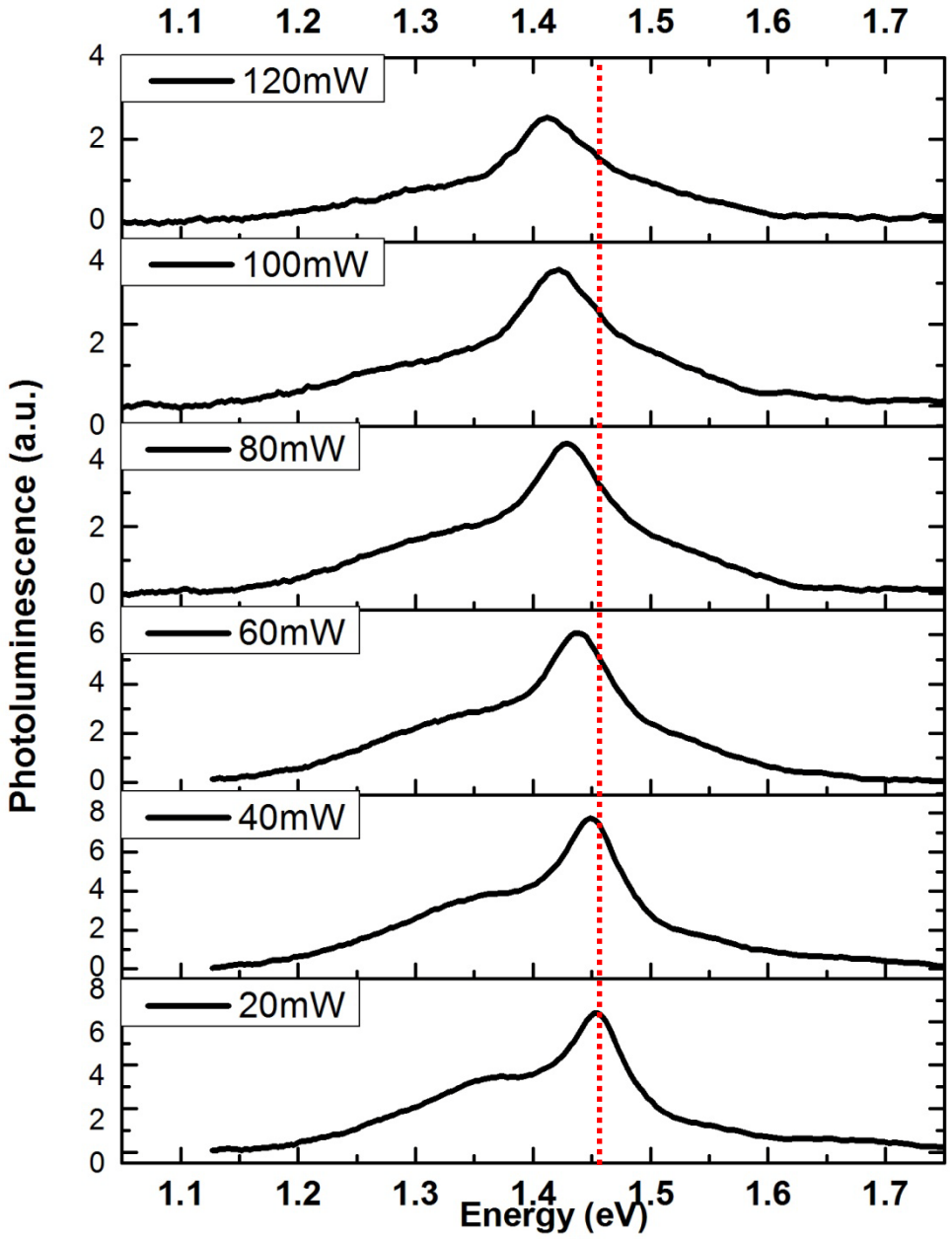

Figure 5.10 Excitation power dependent PL between 20-120 mW at 20 K of 5-stack QRs (droplet forming at 250ºC and crystallization at 250ºC).

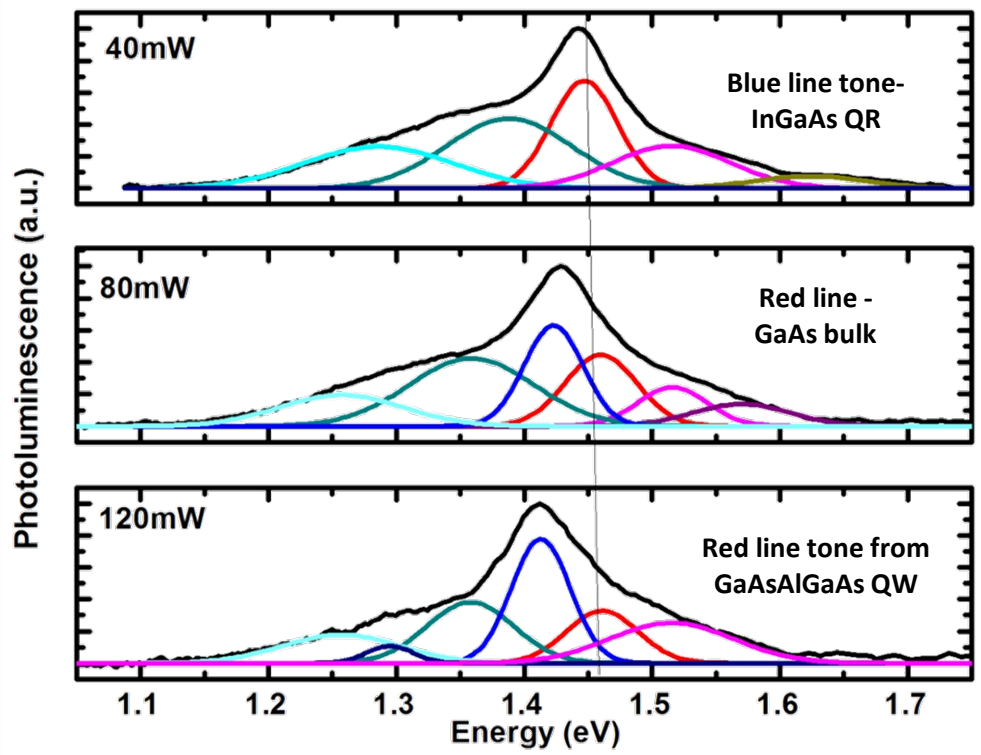

Figure 5.11 Photoluminescence of 5-stack InGaAs QRs (droplet forming at 250ºC and crystallization at 250ºC) with varies excitation power of 40, 80 and 120 mW fitted by series of Gaussian.

5.3 Spectral response measurement

5-stack InGaAs QRs (droplet forming at 350ºC) and 5-stacked InGaAs QRs (droplet forming at 250ºC) are used for analyzing spectral response characteristics. Figure 5.12 shows the normalized spectral responses of the 5-stack InGaAs QRs (droplet forming at 350ºC), and of the reference sample without QRs. It is found that the spectral response of the 5-stack InGaAs QRs (droplet forming at 350ºC) dropped in the 710-890 nm region when it is compared with the response of the reference non-QR sample. The spectral response characteristic from the 5-stack QRs (droplet forming at 350ºC) corresponds to external quantum efficiency of AlGaAs/GaAs QW solar cells [40]. This should be from expansion of Ga and In droplets into 2-dimensional layer. In addition, first 1.75 ML of Ga changes into two-dimensional GaAs layer due to As-

stabilized surface before Ga deposition [31]. It is also supposed to be resulted from very low density of such structures (10^9 QRs/cm^2). Thus, the effect of InGaAs QRs is ineffective for extending spectral absorption.

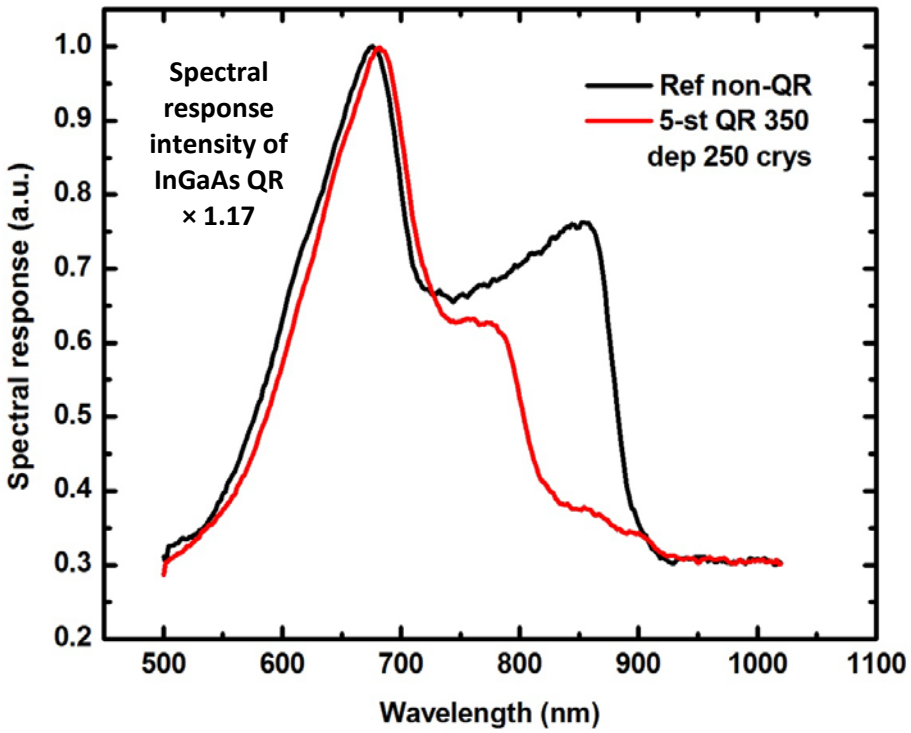

Figure 5.12 Normalized spectral responses for 5-stack InGaAs QR sample with 7.5 ML (droplet forming at 350ºC and crystallization at 250ºC) comparing with the non-QR GaAs reference sample.

A 5-stack of InGaAs QR sample with another InGaAs QR condition (droplet forming at 250ºC and crystallization at 250ºC) is investigated. Figure 5.13 shows spectral response curves of the 5-stack QRs (droplet forming at 250ºC). It is found that the spectral response of this structure gives more photocurrent in the 710-890 nm region than that of reference non-QR and that of 5-stack QRs (droplet forming at 350ºC). It is supposed that the QR (droplet forming at 250ºC) has QR density higher than that of the QR (droplet forming at 350ºC). The longer-wavelength-edge of spectral response from the QRs (droplet forming at 250ºC) is similar to reference sample. This can be explained

by the PL of the QRs (droplet forming at 250ºC). The PL peak of the QRs (droplet forming at 250ºC) is not clearly seen and is closed to the GaAs bulk as shown in Figure 5.12. Thus, the spectral response of the QR (droplet forming at 250ºC) is not clearly extended as in QD and HD-QDM cases.

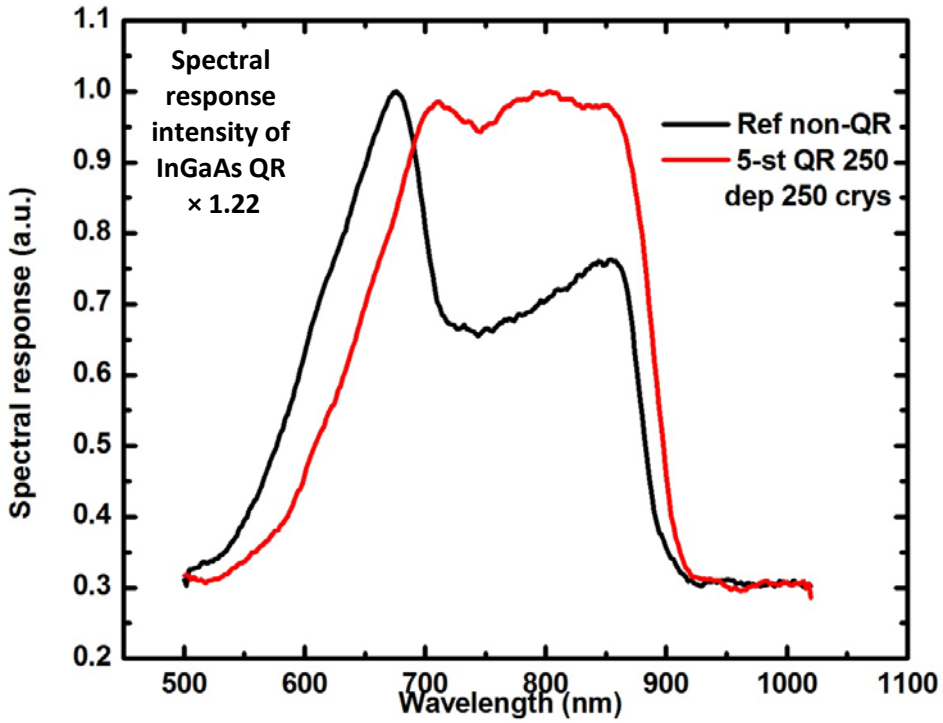

Figure 5.13 Normalized spectral responses for 5-stack InGaAs QR sample with 7.5 ML (droplet forming at 250ºC and crystallization at 250ºC) comparing with the non-QR GaAs/AlGaAs reference sample.

5.4 I-V characterization of QR structure

In order to compare I-V characteristic, another reference sample was grown the same structure but with $Al_{0.3}Ga_{0.7}As$ added in the i-region. Figure 5.14 shows I-V curves of the P-I-N reference sample with various light intensities. It is found that the $V_{cut\text{-}in}$ is 1.15 V which is the same value of the reference cell in chapter 4 which is P-I-N single-heterostructure with $Al_{0.3}Ga_{0.7}As$ added in the n-region. However, the V_{oc} has dropped to 0.55-0.6 V. This dropped is the same phenomena as in the reference cell in chapter 4.

The J_{sc} of the reference cell is 2.39 mA/cm^2 at 1 sun intensity. It is supposed that the AlGaAs in the i-region is a cause of low V_{oc}. The AlGaAs can act as a barrier when electron-hole pairs are generated in the GaAs buffer layer. Thus, J_{sc} of the reference cell is lower than the reference in chapter 4.

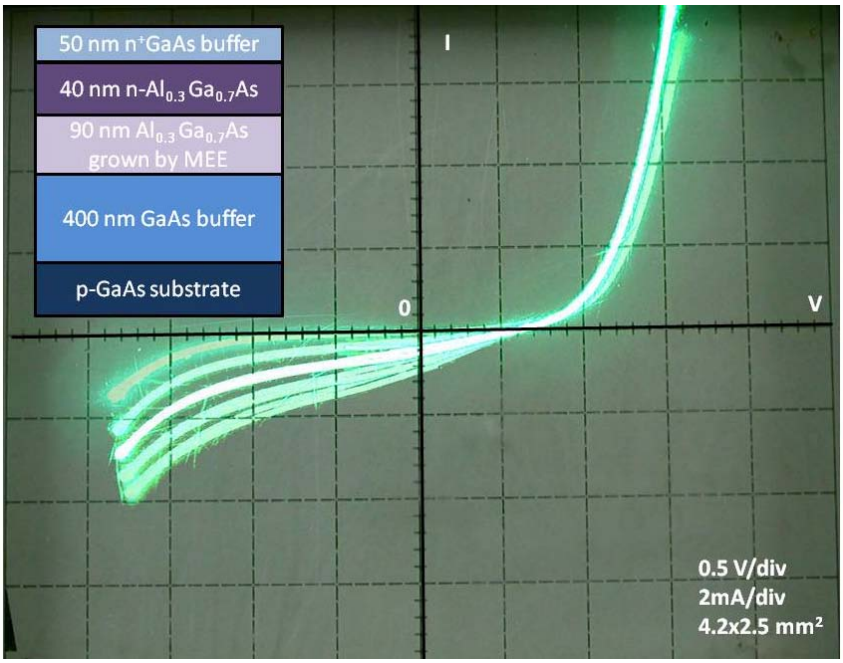

Figure 5.14 I-V curves of GaAs/AlGaAs reference sample with 90 nm AlGaAs grown by MEE in dark condition and 1-4 suns light intensity.

Figure 5.15 and Figure 5.16 show I-V characteristic of the 5-stack InGaAs QRs (droplet forming at 350ºC, crystallization at 250ºC) and I-V characteristic of the 5-stack InGaAs QRs (droplet forming at 250ºC, crystallization at 250ºC), respectively. It is found that the J_{sc} of both structures are in the same value range. However, the photodetector mode in quadrant III, the current density of both structures is increased when compared with the reference cell. These are evidence that the QR structure might give some extra photocurrent.

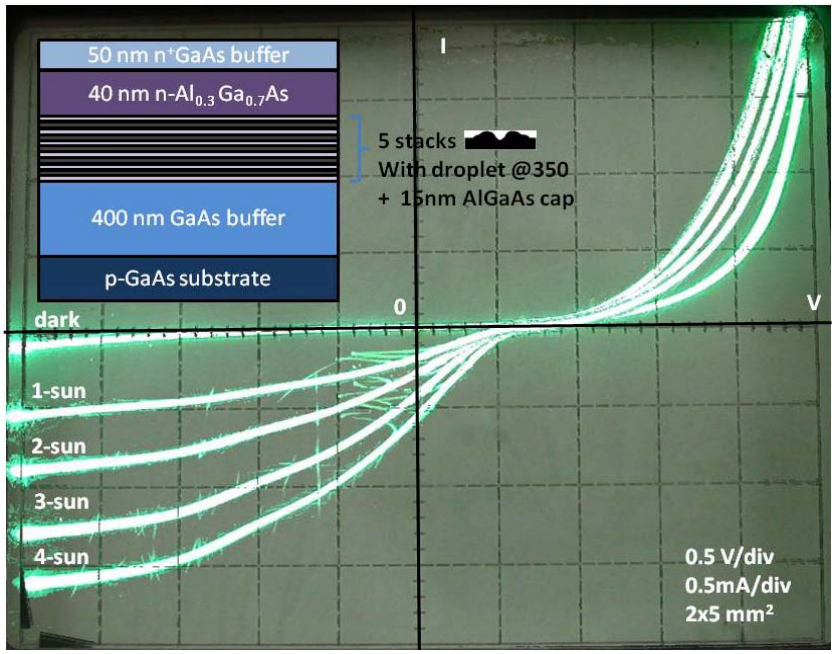

Figure 5.15 I-V curves of 5-stack InGaAs QRs (droplet forming at 350ºC, crystallization at 250ºC) in dark condition and 1-4 suns light intensity.

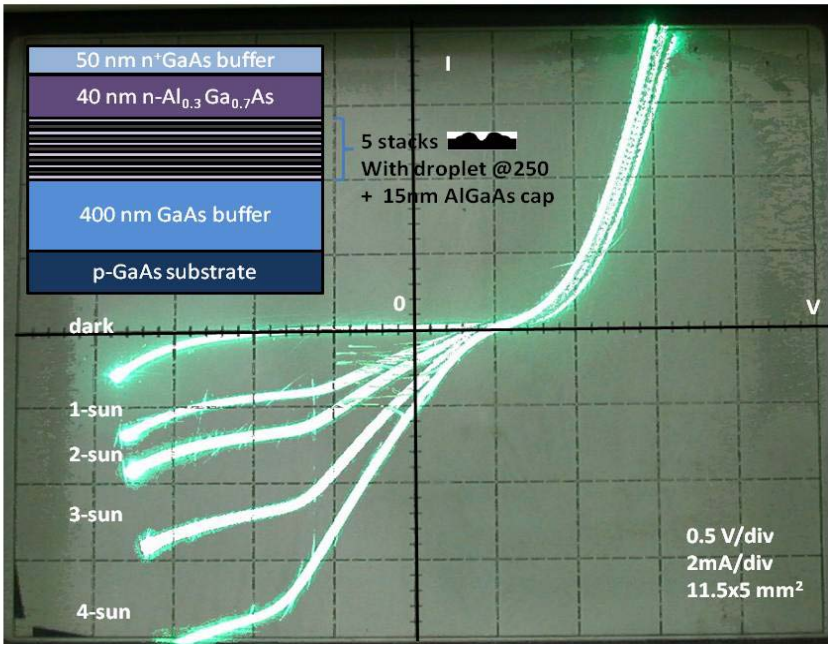

Figure 5.16 I-V curves of 5-stack InGaAs QRs (droplet forming at 250ºC, crystallization at 250ºC) in dark condition and 1-4 suns light intensity.

To prove that the InGaAs QRs can give extra photocurrent, a QR structure is inserted into n-AlGaAs since AlGaAs in the i-region could act as a barrier to block electron flowing from p to n. Thus, n-AlGaAs is used for engineering the energy band. Figure 5.16 shows I-V curves in dark condition and 1-4 suns light intensity of the sample with 5-stack InGaAs QRs in n-AlGaAs (droplet forming at 250ºC, crystallization at 250ºC). $V_{cut\text{-}in}$ of this structure is 0.7 V lower than the other structures. This should be from the n-AlGaAs which is used to confine the barrier of the QR structure. The n-AlGaAs has a lower carrier concentration. This is due to MEE growth which gives a lower carrier concentration than conventional doping growth [72]. When the light illuminates at 1 sun intensity, J_{sc} is ~8 mA/cm^2. J_{sc} is increased when compared to other QR structures and the reference cell. When the light intensity is increased to 2, 3, and 4 suns, J_{sc} increases linearly and gives 32 mA/cm^2 at 4 sun intensity. Thus, the QR structure might be a choice for intermediate band in solar cells.

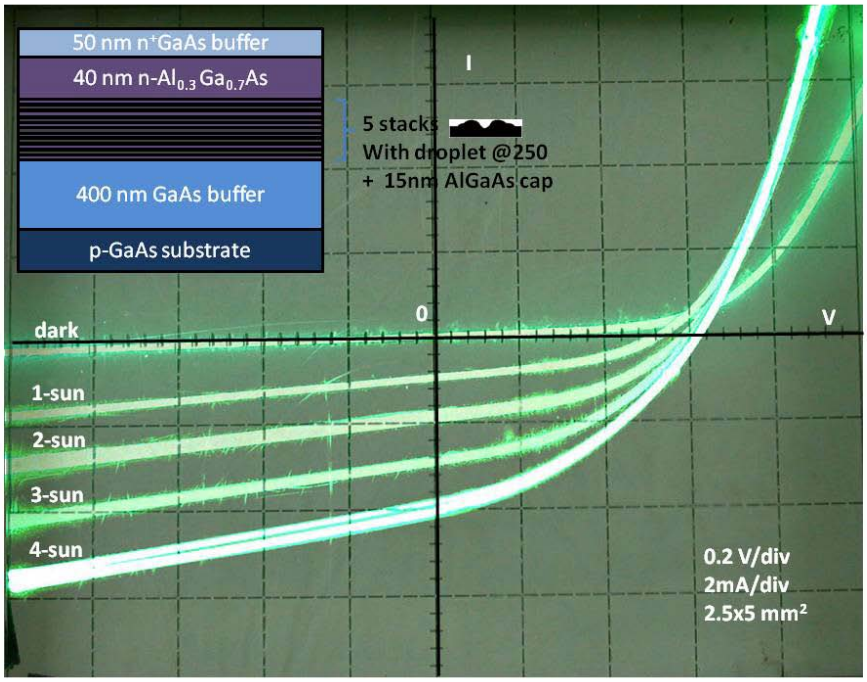

Figure 5.17 I-V curves of 5-stack InGaAs QRs in n-AlGaAs (droplet forming at 250ºC, crystallization at 250ºC) in dark condition and 1-4 suns light intensity.

In this chapter, AFM images of GaAs QRs with various growth conditions are presented. The direction on selecting optimal growth condition is also given. An InGaAs QR layer was inserted instead of GaAs QRs for characterization of the optical and electrical properties. The AFM images of the InGaAs QRs are also shown. The PL result of the InGaAs QR (droplet forming at 350ºC, crystallization at 250ºC) gives a lower PL energy peak than another InGaAs QR condition (droplet forming at 250ºC, crystallization at 250ºC). The spectral response results indicate that 5-stack QR (droplet forming at 350ºC, crystallization at 250ºC) does not show extra photoresponse. The result from 5-stack QR (droplet forming at 350ºC, crystallization at 250ºC) corresponds to an AlGaAs/GaAs QW structure. However, the 5-stack QR (droplet forming at 250ºC, crystallization at 250ºC) gives an extra photo current. This is because it has a higher density per volume than other sample. I-V characteristic results indicate that the 5-stack QR (droplet forming at 250ºC, crystallization at 250ºC) might give a higher current density than the 5-stack QR (droplet forming at 350ºC, crystallization at 250ºC). When QR structure is substituted into n-AlGaAs, the J_{sc} of QR is clearly greater than that of the P-I-N reference cell. Thus, low lattice mismatch QR structure can improve solar cell performance and can be a choice to combine with QD structure for use as an intermediate band solar cell.

CHAPTER VI

CONCLUSIONS

This dissertation presents the photovoltaic effect of nanostructures, i.e., InAs high density quantum dot molecules (HD-QDMs) and InGaAs quantum rings (QRs). The HD-QDMs were grown by using a thin-capping-and-regrowth technique while the QRs were grown by droplet epitaxy. Both structures were fabricated by conventional solid source molecular beam epitaxy.

In order to investigate the properties of HD-QDMs, the quantum dots (QDs) and p-i-n reference samples were used for comparison. The experiment started with optimization of the stacking number of the HD-QDM structure. The HD-QDM photovoltaic devices were Schottky structures for I-V characterization. The result shows that 3-5 stacking number is an optimized range. 3-stack HD-QDMs were chosen for optical and electrical properties characterization.

The PL peak of a 15-stack conventional QD structure has a lower energy than 3-stack HD-QDM structure. The PL results indicate that 3-stack HD-QDMs have less dot uniformity than 15-stack QDs. The PL of the 15-stack QDs has a narrower FWHM than the 3-stack HD-QDMs. When the temperature is increased, the PL spectra of both structures are red-shifted. The PL of the 15-stack QDs is quenched at the high-energy side while the PL emission of the 3-stack HD-QDMs is quite stable at high temperature. This phenomenon from the 15-stack QDs can be explained by thermal activation of carriers from QDs to the GaAs matrix. In contrast, the PL peaks of the HD-QDMs remain broad and unchanged in Gaussian shape at all temperatures. This temperature insensitivity of HD-QDMs is due to close-packing of QDs so that carriers could relax to nearby QDs having different dot sizes. When the incident power excitation is varied, it is found that both structures have similar trend. Thus, the PL of the 15-stack QD structure seems to be composed of many QD sizes. In the 3-stack HD-QDM structure, all QDMs consist of similar dot sizes.

Spectral response results of both structures are extended beyond band edge of GaAs. Spectral response of the 15-stack QDs is narrower than that of 3-stack HD-QDMs. This is due to the higher dot density volume in the shallower active nanostructure. When the light intensity is increased, the extended area of the 15-stack QD sample is stable while the extended area of the 3-stack HD-QDM sample decreases. It implies that the 15-stack QDs have better crystal quality than the 3-stack HD-QDMs. In order to investigate electrical properties, a P-I-N heterostructure is used for observation. I-V results from the p-i-n reference sample indicate that the design of solar cell structure has to be improved. From this experiment, the current density of the reference, the 15-stack QDs and the 3-stack HD-QDMs are close together. However, the current density from 15-stack QD is the highest at concentrated light. Although J_{sc} and V_{oc} from the 15-stack QDs are higher than 3-stack HD-QDMs, it cannot be concluded that QD structure gives better results because the design has to be improved such as thickness of the cell, doping concentration, etc.

Another structure, InGaAs/AlGaAs QRs structure is applied in solar cell structure. In preliminary experiments, GaAs/AlGaAs QR structure is demonstrated to select optimal growth condition. Droplet forming temperature at 350ºC and droplet forming temperature at 250 ºC with crystallization at 250 ºC are used in this experiment. Firstly, single-stack QRs and 5-stack QRs (droplet forming at 350ºC) are compared by PL results. The peak intensity of 5-stack is higher than 1-stack approximate by 4 times. The PL peaks of both sample InGaAs QR samples have the same position. The 5-stack InGaAs QRs of both growth conditions were fabricated for investigating optical and electrical properties.

The PL peak of the 5-stack QRs (droplet deposition at 350ºC) is clearly observed while the PL peak of the 5-stack QR (droplet deposition at 250ºC) has merged with the GaAs peak. The FWHM of both structures is broad when compared with the QD and HD-QDM structure. With highly increased temperature, the PL spectrum of the QRs becomes hardly detectable. This is due to the non-perfect crystal quality and the low density of the QRs. However, the PL of the 5-stack QRs (droplet deposition at 250ºC)

exhibits higher temperature than the PL of 5-stack QRs (deposition at 350 ºC) probably because it has a higher density per unit volume than 5-stack QRs (deposition at 350 ºC). The PL of the 5-stack QRs (droplet forming at 350 ºC) is unchanged with incident power while that of 5-stack QRs (droplet forming at 250 ºC) is red-shifted when the power excitation is increased. This might be due to the band filling effect in 5-stack QRs (droplet forming at 250 ºC).

Spectral response results of 5-stack QRs (droplet forming at 350 ºC) correspond to the external quantum efficiency of AlGaAs/GaAs QW solar cells while that of 5-stack QRs (droplet forming at 350 ºC) does not. The spectral response from the 5-stack QRs (droplet deposition at 250 ºC) gives more photo current in the 710-890 nm region the than reference non-QR and 5-stack QRs (droplet forming at 350 ºC). However, the spectral response of both 5-stacked QR is not clearly extended as in the QD and HD-QDM cases. I-V characteristic results indicate that the 5-stack QRs (droplet forming at 250ºC) might give a higher current density than the 5-stack QRs (droplet forming at 350ºC). When a QR structure is inserted into n-AlGaAs, the J_{sc} of the QR is clearly greater than that of the reference cell. Thus, it can be concluded that QRs (droplet forming at 250ºC), which have a higher density and smaller size, are better in solar cells than QRs (droplet forming at 350ºC). It also can improve solar cell performance and can be a choice to combine with QD structure in an intermediate band solar cell.

Recommendations for further work

A proper design of the solar cell structure should be further studied to improve device performance. Due to the wider range of the spectral response of HD-QDM, the HD-QDM is a promising structure for high photocurrent density device. Thus, the design of the insertion of a HD-QDM structure has to be improved for used in a solar cell structure, such as increase thickness spacing of the HD-QDM structure which might increase the stacking number of HD-QDM. InGaAs/AlGaAs QR or GaAs/AlGaAs might be utilized to improve the V_{oc} and J_{sc} with an optimization HD-QDM condition. This is because both structures have low strain. In multi-stack InGaAs/AlGaAs, it is also shown

that QR sample gives higher J_{sc} than reference non-QR. Thus, QRs might improve the solar cell efficiency when they are combined with the HD-QDM solar cell structure.

REFERENCE

[1] Knobloch, J., Glunz, S.W., Biro, D., Warta, W., Schaffer, E., and Wettling, W. SOLAR CELLS WITH EFFICIENCIES ABOVE 21% PROCESSED FROM CZOCHRALSKI GROWN SILICON. IEEE proceeding of 25th PVSC (1996): 405-408.

[2] Zhou, C. Z., Verlinden, P. J., Crane, R. A., and Swanson, R. M. 21.9% EFFICIENT SILICON BIFACIAL SOLAR CELLS. IEEE proceeding of 26th PVSC (1997): 287-290.

[3] Zhao, J., Wang, A., and Green, M.A. 24.5% Efficiency Silicon PERT Cells on MCZ Substrates and 24.7% Efficiency PERL Cells on FZ Substrates. PROGRESS IN PHOTOVOLTAICS: RESEARCH AND APPLICATIONS 7 (1999): 471-474.

[4] Jagannathan, B., Anderson, W.A., and Coleman, J. Amorphous silicon/p-type crystalline silicon heterojunction solar cells. Solar Energy Material and Solar Cells 46 (1997): 289-310.

[5] Blakers, A. W. Substrates for thin crystalline silicon solar cells. Solar Energy Material and Solar Cells 51 (1998): 385-392.

[6] Song, Y.J., and Anderson, W.A. Amorphous silicon/p-type crystalline silicon heterojunction solar cells with a microcrystalline silicon buffer layer. Solar Energy Material and Solar Cells 64 (2000): 241-249.

[7] Shockley, W., and Queisser, H. J. Detailed Balance Limit of Efficiency of p-n Junction Solar Cells. Journal of Applied Physics 32 (1961): 510-519.

[8] Vos, A. D. Detailed balance limit of the efficiency of tandem solar cells. Journal of Physics D: Applied Physics13, 5 (1980): 839-846.

[9] Nishioka, K., Takamoto, T., Agui, T., Kaneiwa, M., Uraoka, Y., and Fuyuki, T.Evaluation of InGaP/InGaAs/Ge triple-junction solar cell and optimization of solar cell's structure focusing on series resistance for high-efficiency concentrator photovoltaic systems. Solar Energy Material and Solar Cells90 (2006): 1308–1321.

[10] Takeda, Y., and Motohiro, T. Highly efficient solar cells using hot carriers generated by two-step excitation. Solar Energy Material and Solar Cells 95 (2011): 2638–2644.

[11] Landsberg, P. T., Nussbaumer, H., and Willeke, G. Band-band impact ionization and solar cell efficiency. Journal of Applied Physics 74 (1993):1451-1452.

[12] Luque, A., and Marti, A. Increasing the Efficiency of Ideal Solar Cells by Photon Induced Transitions at Intermediate Levels. Physical Review Letters 26 (1997): 5014–5017.

[13] CLEANTECHNICA NEWS FEATURE. .Avalable from : http://cleantechnica.com/2011/04/19/solar-junction-breaks-concentrated-solar-world-record-with-43-5-efficiency/

[14] Nozawa, T., and Arakawa, Y. Detailed balance limit of the efficiency of multilevel intermediate band solar cells. Applied Physics Letters 98. (2011): 171108-171110.

[15] Reed M.A., Randall J.N., Aggarwal R.J., Matyi R.J., Moore T.M., and Wetsel A.E. Observation of Discrete Electron states in a Zero-Dimensional Semiconductor Nanostructure. Physical Review Letters 60 (1988): 535–537.

[16] Bimberg, D., Grundmann, M., and Leddentsov, N.N. Quantum dot Heterostructures: Chichester Wiley, 1999.

[17] Grutzmacher, D., et al. Three-Dimensional Si/Ge Quantum Dot Crystals. Nano Letters 7, 10 (2007): 3150-3156.

[18] Baier, M. H., Watanabe, S., Pelucchi, E., and Kapon, E. High uniformity of site-controlled pyramidal quantum dots grown on prepatterned substrates. Applied Physics Letters 84 (2004): 1943-1945.

[19] Kiravittaya, S., Rastelli, A., and Schmidt, O. G. Photoluminescence from seeded three-dimensional InAs/GaAs quantum-dot crystals. Applied Physics Letters 88 (2006): 43112-43114.

[20] Heinrichsdorff, F., Krost, A., Grundmann, M., and Bimberg, D. Self-organization processes of InGaAs/GaAs quantum dots grown by metalorganic chemical vapor deposition. Applied Physics Letters 68, 23 (1996): 3284-3286.

[21] Nuntawong, N., Birudavolu, S., Hains, C.P., Huang, S., Xu, H., and Huffaker, D. L. Effect of strain-compensation in stacked 1.3 mm InAs/GaAs quantum dot active regions grown by metalorganic chemical vapor deposition. Applied Physics Letters85 (1994): 3050-3052.

[22] Hubbard, S. M., Cress, C. D., Bailey, C. G., Raffaelle, R. P., Bailey, S. G., and Wilt, D. M. Effect of strain compensation on quantum dot enhanced GaAs solar cells. Applied Physics Letters 92 (2008): 123512-123514.

[23] Okada, Y. Oshima, R., and Takata, A. Characteristics of InAs/GaNAs strain-compensated quantum dot solar cell. Journal of Applied Physics 106 (2009): 24306-24308.

[24] Suraprapapich, S., Kanjanachuchai, S., Thainoi, S., and Panyakeow, S. Regrowth of self-assembled InAs quantum dots on nanohole and stripe templates. Journal of Microlithography, Microfabrication, and Microsystems 5 (2006): 11008-11012.

[25] Suraprapapich, S., Thainoi, S., Kanjanachuchai, S., and Panyakeow, S. Self-assembled quantum-dot molecules by molecular-beam epitaxy. Journal of Vacuum Science and Technology B. 23 (2005): 1217-1220.

[26] Luque, A., et al. General equivalent circuit for intermediate band devices: Potentials, currents and electroluminescence. Journal of Applied Physics 96 (2004): 903-909.

[27] Marti, A., et al. Emitter degradation in quantum dot intermediate band solar cells. Applied Physics Letters 90 (2007) 233510-233513.

[28] Zhou, D., Sharma, G., Thomassen, S. F., Reenaas, T. W., and Fimland, B. O. Optimization towards high density quantum dots for intermediate band solar cells grown by molecular beam epitaxy. Applied Physics Letters, 96 (2010): 61913-61915.

[29] Sablon, K. A., et al. Effects of AlGaAs energy barriers on InAs/GaAs quantum dot solar cells. Journal of Applied Physics 108 (2010): 74305-74308.

[30] Bailey,C.G., Forbes,D.V., Raffaelle, R. P., and Hubbard, S.M. Near 1 V open circuit voltage InAs/GaAs quantum dot solar cells. Applied Physics Letters 98 (2011): 163105-163107.

[31] Mano, T., and Koguchi, N. Nanometer-scale GaAs ring structure grown by droplet epitaxy. Journal of Crystal Growth 278 (2005): 108-112.

[32] Mano, T., et al. Self-Assembly of Concentric Quantum Double Rings. Nano Letters 5 (2005): 425-428.

[33] Mano, T., Watanabe, K., Tsukamoto, S., Fujioka, H., Oshima, M., and Koguchi, N. Fabrication of InGaAs quantum dots on GaAs(0 0 1) by droplet epitaxy. Journal of Crystal Growth 209 (2000) : 504-508.

[34] King, R. R., et al. Band gap-voltage offset and energy production in next-generation multijunction solar cells. PROGRESS IN PHOTOVOLTAICS: RESEARCH AND APPLICATIONS 19 (2010): 797–812

[35] Geisz, J.F., et al. High-efficiency GaInP/GaAs/InGaAs triple-junction solar cells grown inverted with a metamorphic bottom junction. Applied Physics Letters 91 (2007) : 23502-23504.

[36] Wei, G.,and Forrest, S.R. Intermediate-Band Solar Cells Employing Quantum Dots Embedded in an Energy Fence Barrier. Nano Letters 7 (2007): 218-222.

[37] Laghumavarapu, R.B., El-Emawy, M., Nuntawong, N., Moscho, A., Lester, L.F., and Huffaker, D.L. Improved device performance of InAs/GaAs quantum dot solar cells with GaP strain compensation layers. Applied Physics Letters 91 (2007): 243115-243117.

[38] Keevers, M.J., and Green, M.A. Efficiency improvements of silicon solar cells by the impurity photovoltaic effect. Journal of Applied Physics 75 (1994): 4022-4031.

[39] Keevers, M.J., and Green, M.A. Extended infrared response of silicon solar cells and the impurity photovoltaic effect. Solar Energy Material and Solar Cells 41 (1996):195-204.

[40] Bamham, K. , et al. Quantum well solar cells. Applied Surface Science 113 (1997): 722-733.

[41] Wei, G., Shiu, K.-T., Giebink, N.C., and Forrest, S.R. Thermodynamic limits of quantum photovoltaic cell efficiency. Applied Physics Letters 91 (2007): 223507-223509.

[42] Popescu, V., Bester, G., Hanna, M.C., Norman, A.G., and Zunger, A. Theoretical and experimental examination of the intermediate-band concept for strain-balanced (In,Ga)As/Ga(As,P) quantum dot solar cells. Physical Review B 78 (2008): 205321-1-205321-17.

[43] Marti, A., et al. Elements of the design and analysis of quantum-dot intermediate band solar cells. Thin Solid Films (2008): 6716–6722.

[44] Tomic, S., Marti, A., Antolin, E., and Luque A. On inhibiting Auger intraband relaxation in InAs/GaAs quantum dot intermediate band solar cells. Applied Physics Letters, 99 (2011): 53504-53506.

[45] Luque, A., et al.E. New Hamiltonian for a better understanding of the quantum dot intermediate band solar cells. Solar Energy Material and Solar Cells 95 (2011): 2095–2101.

[46] Hubbard, S.M., et al. INAS QUANTUM DOT ENHANCEMENT OF GAAS SOLAR CELLS. IEEE proceeding of 35th PVSC (2010): 1217- 1222.

[47] Sugaya, T., et al. Highly stacked and well-aligned In0.4Ga0.6As quantum dot solar cells with In0.2Ga0.8As cap layer. Applied Physics Letters 97 (2010): 183104-183106.

[48] Sablon, K.A., Little, J.W., Mitin, W., Sergeev, A., Vagidov, N., and Reinhardt, K. Strong Enhancement of Solar Cell Efficiency Due to Quantum Dots with Built-In Charge. Nano Letters 11 (2011): 2311–2317.

[49] Guimard, D., et al. Fabrication of InAs/GaAs quantum dot solar cells with enhanced photocurrent and without degradation of open circuit voltage. Applied Physics Letters 96 (2010): 203507-203509.

[50] Sugawara, M. Theoretical Bases of the optical Properties of Semiconductor Quantum Nano-structures. Semiconductors and Semimetals : Self-Assembled InGaAs/GaAs Quantum Dots,60, pp.1–116, San Diego: Academic Press, 1999.

[51] Seifert, W., Carlsson, N., Johansson, J., Pistol, M.E. and Samuelson L. In situ growth of nano-structures by metal-organic vapour phase epitaxy. Journal of CrystalGrowth, 170 (1997): 39-46.

[52] Suwit Kirawittaya, Homogeneity improvement of InAs/GaAs self-assembled quantum dots grown by molecular beam epitaxy, Doctoral Thesis, Department of Electrical Engineering Faculty of Engineering Chulalongkorn University, 2002.

[53] Kim, J., et al. Different shape of GaAs quantum structures under various growth conditions. Thin Solid Films 518 (2010): 6500–6504.

[54] Lee, J.H., Wang, Zh. M., Kim, E.S., Kim, N.Y., Park, S.H., and Salamo, G.J. Various Quantum- and Nano-Structures by III–V Droplet Epitaxy on GaAs Substrates. Nanoscale Research Letters 5 (2010): 308.

[55] Abbarchi, M., et al. Micro-photoluminescence of GaAs/AlGaAs triple concentric quantum rings. Nanoscale Research Letters 6 (2011): 569.

[56] Herman, M.A., and Sitter, H. Molecular beam epitaxy fundamentals and current status, Berlin: Spinger-Verleg, 1989.

[57] Kim, J.H., et al. Growth and characterization of GaAs layers on Si substrates by migration-enhanced molecular beam epitaxy Applied Physics Letters 53 (1988): 2435-2437.

[58] H. Ibach and H. Lueth. *Solid-State Physics*. Springer Verlag, 2003. Abalable from : http://gorgia.no-ip.com/phd/html/thesis/phd_html/node4.html

[59] Franchi, S., Trevisi, G., Seravalli, L., and Frigeri, P. Quantum dot nanostructures and molecular beam epitaxy. Progress in Crystal Growth and Characterization of Materials, 47 (2003): 166-195.

[60] Varshni, Y.P. Temperature dependence of the energy gap in semiconductors. Physica E 34 (1967): 149–154.

[61] Ng, J., and Missous, M. Improvements of stacked self-assembled InAs/GaAs quantum dot structures for 1.3μm applications. Microelectronics Journal 37 (2006) :1446-1450.

[62] Grundmann, M., and Bimberg, D. Theory of random population for quantum dots. Physical Review B 55 (1997): 9740–9745.

[63] Bhattacharya, P. Semiconductor Optoelectronic Devices: Prentice-Hall,Inc, 1994.

[64] Mano, T., Noda, T., Yamagiwa, M., and Koguchi, N. Coupled quantum nanostructures formed by droplet epitaxy. Thin Film Solids 515 (2006): 531-534.

[65] Pankaow, N., Panyakeow, S., and Ratanathammaphan, S. Nanometer-scale $In_{0.5}Ga_{0.5}As$ ring-like structure grown by droplet epitaxy. Advanced Materials Research 31 (2008): 123-125.

[66] Pankaow, N., Panyakeow, S., and Ratanathammaphan, S. Formation of $In_{0.5}Ga_{0.5}As$ ring-and-hole structure by droplet molecular beam epitaxy. Journal of Crystal Growth 311 (2009): 1832-1835.

[67] Wu, J., et al. Intermediate-band material based on GaAs quantum rings for solar cells. APPLIED PHYSICS LETTERS 95 (2009): 71908-71910.

[68] Jevasuwan, W., Boonpeng, P., Panyakeow, S., and Ratanathammaphan, S. Influence of crystallization temperature on InP ring-shaped quantum-dot molecules grown by droplet epitaxy. Microelectronic Engineering 87 (2010): 1416–1419.

[69] Poonyasiri Boonpeng. Fabrication of self-assembled InGaAs nanostructures grown by droplet epitaxy using molecular beam epitaxy for quantum dot molecules. Doctor's Thesis, Department of Electrical Engineering Faculty of Engineering Chulalongkorn University, 2010.

[70] Sanguinetti, S., et al. Rapid thermal annealing effects on self-assembled quantum dot and quantum ring structures, Journal of Applied Physics 104 (2008): 113519-113523.

[71] Mano, T. et al. Ring-shaped GaAs quantum dot laser grown by droplet epitaxy: Effects of post-growth annealing on structural and optical properties. Journal of Crystal Growth 301-302 (2007): 740-743.

[72] Tadayon, B., Tadayon, S., Spencer, M.G., Harris, G.L., Griffin, J.,and Eastman, L.F. Increase of electrical activation and mobility of Si doped GaAs, grown at low substrate temperatures, by the migrationenhanced epitaxy method. Journal of Applied Physics 67 (1990): 589- 591.

APPENDIX

LIST OF PUBLICATIONS

1. N. Chit Swe, **O. Tangmattajittakul**, S. Suraprapapich, P. Changmuang, S. Thainoi, C. Wissawinthanon, S. Kanjanachuchai, S. Ratanathammaphan, and S. Panyakeow 2008. Improve quantum confinement of self- assemble high-density InAs quantum dot molecules in ALGaAs/GaAs quantum well structure by molecular beam epitaxy. Journal of Vacuum Science Technology B. 26 : 1100-1104.
2. K. Laouthaiwattana, **O. Tangmattajittakul**, S. Suraprapapich, S. Thainoi, P. Changmuang, S. Kanjanachuchai, S. Ratanathammaphan, and S. Panyakeow 2009. Optimization of stacking high densityquantumdot molecules for photovoltaic effect. Solar Energy Materials & SolarCells, 93 : 746-749.
3. **O. Tangmettajittakul**, S. Thainoi, P. Changmoang, S. Kanjanachuchai, S. Rattanathammaphan, and S. Panyakeow, 2010. Extended Optical Properties beyond Band- Edge of GaAs by InAs Quantum dots and Quantum Dot Molecules. Microelectronic Engineering. 87 : 1304-1307.
4. **O.Tangmettajittakul**, S. Thainoi, S. Panyakeow, and S. Rattanathammaphan 2010. A Si-doped GaAs/AlGaAs Solar cell on (311) A GaAs Substrate. CompoundSemiconductor Photonics. : 149-151.
5. **O. Tangmettajittakul**, P. Changmoang, S. Thainoi, S. Kanjanachuchai, S. Ratanathammaphan, and S. Panyakeow 2010. Improved Spectral Response of Quantum Dot Solar Cells Using InAs Multi-stack High Density Quantum Dot Molecules. MRS Symposium proceedings. 1260, 101-105.
6. **O. Tangmetajitakul**, S. Thainoi, P. Changmoang, S. Kanjanachuchai, S. Rattanathammaphan, and S. Panyakeow 2010. Study on Spectral Responses of Schottky-Type Multi-Stack High Density Quantum Dot Molecule Photovoltaic Cells at

Concentrated Light. Photovoltaic Spacialists Conference (PVSC),2010 35th IEEE. : 001838-001842.

7. **O. Tangmetajitakul**, S. Thainoi, S. Panyakeow, and S. Rattanathammaphan, 2012 Evolution of self assembled InAs quantum dot molecules by molecular beam epitaxy, Special Issue in Phisica Status Solidi (C) Article In Press.

LIST OF PRESENTATION

1. N. Chit Swe, **O. Tangmattajittakul**, S. Suraprapapich, P. Changmuang, S. Thainoi, C. Wissawinthanon, S. Kanjanachuchai, S. Ratanathammaphan, and S. Panyakeow Improve quantum confinement of self-assemble high-density InAs quantum dot molecules in ALGaAs/GaAs quantum well structure by molecular beam epitaxy 2007. 25th North American Conference on Molecular Beam Epitaxy(NAMBE2007), 23-26,9, 2007, Albuquerque, New Mexico, USA.
2. K. Laouthaiwattana, **O. Tangmattajittakul**, S. Suraprapapich, S. Thainoi, P. Changmuang, S. Kanjanachuchai, S. Ratanathammaphan, and S. Panyakeow Optimization of stacking high-density quantumdot molecules for photovoltaic effect 2007. 17th International Photovoltaic Science and Engineering Conference PVSEC-17, 3- 7/12/2007, Fukuoka, Japan.
3. **O. Tangmettajittakul**, S. Thainoi, P. Changmoang, S. Kanjanachuchai, S. Rattanathammaphan, and S. Panyakeow Extended Optical Properties beyond Band-Edge of GaAs by InAs Quantum dots and Quantum Dot Molecules 2009. International Conference on Micro & Nano Engineering, 28/9-1/10 2009, Ghent, Belgium.
4. **O. Tangmettajittakul**, S. Thainoi, S. Panyakeow, and S. Rattanathammaphan A Si-doped GaAs/AlGaAs Solar cell on (311) A GaAs Substrate 2009. International Conferrence on Materials for Advanced Technologies,(ICMAT 2009), 28/6-3/7 2009, Singapore.
5. **O. Tangmettajittakul**, S. Thainoi, S. Panyakeow, and S. Rattanathammaphan Effect of Si effusion cell temperature on Si-doped p-n (311)A GaAs photovoltaic cell 2009. Electrical Engineering conf.(EECON 32), 28- 30/10/ 2009, Pracheenburi, Thailand.
6. **O. Tangmettajittakul**, P. Changmoang, S. Thainoi, S. Kanjanachuchai,

S. Ratanathammaphan, and S. Panyakeow Improved Spectral Response of Quantum Dot Solar Cells Using InAs Multi-stack High Density Quantum Dot Molecules 2010. MRS Spring Meeting, 5-9/4/ 2010, SanFrancisco, USA.

7. **O. Tangmetajitakul**, S. Thainoi, P. Changmoang, S. Kanjanachuchai, S. Rattanathammaphan, and S. Panyakeow Study on Spectral Responses of Schottky-Type Multi-Stack High Density Quantum Dot Molecule Photovoltaic Cells at Concentrated Light 2010. 35th IEEE Photovoltaic srecialist conference, 20-25/6/2010, Hawai, USA.
8. **O. Tangmetajitakul**, S. Thainoi, P. Changmoang, S. Kanjanachuchai, S. Rattanathammaphan, and S. Panyakeow MBE growth process and PL characterization of multi-stack QD and multi-stack HD-QDM 2010. 16th Intermational Conference on Molecular Beam Epitaxy (MBE 2010), 22-27/8/2010, Berlin, Germany.
9. **O. Tangmetajitakul**, S. Thainoi, P. Changmoang, S. Rattanathammaphan, and S. Panyakeow Utilization of GaAs/AlGaAs Quantum Rings in Solar Cell Structure 2011. Photovoltaic Technical Conference, 25-27/5/2011, Aix-en, France.
10. **O. Tangmetajitakul**, P. Boonpeng, S. Thainoi, P. Changmoang, S. Rattanathammaphan, and S. Panyakeow GaAs/AlGaAs Quantum Nanostructure by Droplet Epitaxy for Photovoltaic Application 2011. 37th IEEE Photovoltaic srecialist conference, 19-24/6/2011, Saettle, Washington, USA.
11. **O. Tangmetajitakul**, S.Thainoi, S. Panyakeow, and S. Rattanathammaphan Evolution of self assembled InAs quantum dot molecules by molecular beam epitaxy 2011. 16th Semiconducting and Insulating Materials Conference (SIMC-XVI), 19-23/6/2011, Stockholm, Sweden.
12. **O. Tangmetajitakul**, S.Thainoi, Rattanathammaphan, and S. Panyakeow Integration of InGaAs/AlGaAs Quantum Ring to solar cell structure 2011. 21 International

Photovoltaic Science and Engineering Conference PVSEC-21, 28/11-2/12/2011, Fukuoka, Japan.

13. P. Prongjit, **O. Tangmettajittakul**, S.Thainoi, N. Pankaow, S. Panyakeow, and S. Rattanathammaphan, Fabrication of GaP Nanostructure on GaAs (100) by Droplet Molecular beam Epitaxy, The 28th NAMBE, 14-17/8/2011, University of California San Diego, La Jolla, CA, U.S.A.
14. **O. Tangmettajittakul**, S. Panyakeow, and S. Ratanathammaphan, Study on Photovoltaic effect of quantum nanostructure grown on (100) GaAs substrate (Outstanding Poster Presentation Award), RGJ-Ph.D. Congress XII, 1-2/4/2012, Pattaya, Thailand

VITAE

Ong-arj Tangmettajittakul was born in Bangkok, Thailand on June 19, 1982. In june 2002, he entered King Mongkut's University of Technology Thonburi (KMUTT) and received Bachelor of Electronics and Telecommunication Engineering in 2005. In June 2005, he entered the Graduate School of Chulalongkorn University and become the Master student in Electrical Engineering Program at Semiconductor Device Research Laboratory (SDRL). He received the Master degree of Electrical Engineering in May 2007. Then, he studied as a Ph.D. student t the same place. His research work is financial supported by Thailand Research Fund (TRF) through the Royal Golden Jubilee (RGJ) (Grant number PHD/0017/2552).